**Weierstraß-Institut
für Angewandte Analysis und Stochastik
Leibniz-Institut im Forschungsverbund Berlin e. V.**

Preprint ISSN 2198-5855

An asymptotic model of the Poisson–Nernst–Planck–Stokes system for ion transport in narrow channels

Christine Keller[1], Barbara Wagner[1], Andreas Münch[2]

submitted: December 11, 2025

[1] Weierstrass Institute
Anton-Wilhelm-Amo-Str. 39
10117 Berlin
Germany
E-Mail: christine.keller@wias-berlin.de
barbara.wagner@wias-berlin.de

[2] Mathematical Institute
University of Oxford
Woodstock Road
Oxford, OX2 6GG, UK
E-Mail: muench@maths.ox.ac.uk

No. 3243
Berlin 2025

2020 *Mathematics Subject Classification.* 35Q35, 35Q92, 76D08, 76M45, 80A30, 92C05.

Key words and phrases. Asymptotic analysis, lubrication theory, Poisson-Nernst-Planck-Stokes, nanopores, ion transport.

C.K. gratefully acknowledges the financial support by the Deutsche Forschungsgemeinschaft (DFG, German Research Foundation) under Germany's Excellence Strategy – The Berlin Mathematics Research Center MATH+ (EXC-2046/1, project ID: 390685689) via the project AA1-14.

Edited by
Weierstraß-Institut für Angewandte Analysis und Stochastik (WIAS)
Leibniz-Institut im Forschungsverbund Berlin e. V.
Anton-Wilhelm-Amo-Str. 39
10117 Berlin
Germany

Fax: +49 30 20372-303
E-Mail: preprint@wias-berlin.de
World Wide Web: http://www.wias-berlin.de/

An asymptotic model of the Poisson–Nernst–Planck–Stokes system for ion transport in narrow channels

Christine Keller, Barbara Wagner, Andreas Münch

Abstract

Ion transport through narrow channels is determined by the interaction between electrochemical and hydrodynamic effects, which are influenced by the channel geometry, ion concentrations, pressure and potential gradients, and surface charges. Understanding the mechanisms that control electrokinetic phenomena such as ion selectivity and flow transitions is crucial for elucidating biological functions and for further developing the design of artificial nanofluidic systems. On the continuum scale, these processes are described by the coupled Poisson-Nernst-Planck-Stokes equations (PNPS). However, direct numerical simulations in two or three dimensions are computationally intensive and provide only limited insights into the underlying physical and mathematical structure. Taking advantage of the small aspect ratio characteristic of nanopores, we derive a systematic asymptotic reduction of the PNPS boundary value problem. In contrast to existing one-dimensional reductions, which assume a Debye length much smaller than the channel radius, our analysis identifies a distinct asymptotic regime in which the Debye length is comparable to the channel width. This framework extends the applicability of reduced PNPS models and recovers previous approximations as limiting cases. The resulting model provides clarity and predictability for a wide range of settings. We demonstrate the influence of geometry and flow on ion transport in trumpet-shaped nanopores, flow transitions that occur due to electrostatic and hydrodynamic forces, and the conductivity properties of a protein-based channel.

1 Introduction

Nanopores are nanoscale channels that play an important role in both biology and technical applications. Biological nanopores, also referred to as ion channels, are pore-forming proteins in cell membranes and are involved in many physiological functions. They regulate the exchange of ions across the otherwise impermeable lipid bilayer and are able to discriminate between different molecules based on size, charge and structure. Synthetic nanopores on the other hand are made of solid-state materials such as silicon, nitride, graphene, glass or polymeres and highly customizable. They are used in a variety of applications such as protein and DNA sensing [3, 23, 30, 36, 37], water filtration and desalination [4, 18, 29, 35] and many more.

The transport in ion channels is controlled by a highly complex interplay of forces, including the specific geometry of the channels, ion concentrations, concentration gradients, the pressure exerted on the channel, and surface conditions such as charge patterns on the channel surface. A crucial aspect in this context is the interaction between ion transport and fluid flow, especially in the presence of an external electric field and charged pore walls. The interplay of these factors leads to electroosmotic flow (EOF), a phenomenon in which the movement of ions in an applied field triggers fluid flow within the nanopore. EOF helps to control the translocation of molecules (such as DNA or small proteins) through the pore, improving sequencing and sensor applications [3, 30].

DOI 10.20347/WIAS.PREPRINT.3243 Berlin 2025

It is therefore of great importance to understand how the dominant driving force can be shifted from EOF to a hydrodynamic flow and vice versa by adjusting the salt concentrations or the properties of the pores [4, 30]. For example, geometric asymmetries can lead to ion current rectification, i.e., asymmetries in the measured current-voltage curves [8, 15, 33]. Surface charge patterns in channels can also qualitatively alter electroosmotic flows due to the coupling between hydrodynamic flow and electrostatic interactions [2, 14, 16, 34]. Many of these phenomena occur naturally in biological ion channels [1, 5, 12, 19, 39], and a deeper understanding of the underlying electrohydrodynamic system not only clarifies their modes of operation but also provides fundamental insights for the development of new artificial micro- or nanofluidic devices.

Current-voltage (IV) relations provide important information about ion transport in nanopores. They can provide information about conductivity or the effects of EOF under varying conditions such as different ion concentrations, surface charges and geometries. The interpretation of IV curves is therefore crucial for many applications and can help in the development and optimization of devices.

Mathematical modeling can be used to quantify how ion concentration gradients, applied voltage and surface charge influence the flow of ions through the pore. To model ion electro-diffusion the Poisson-Nernst-Planck (PNP) equations are commonly used. This set of equations combines the Poisson equation which describes the electrostatic potential with the Nernst-Planck equations, describing the movement of ions due to diffusion and drift due to electrostatic forces. Coupling PNP with Stokes equations allows to capture the movement of the solvent (e.g. water) due to the electric field [7, 10, 13, 14, 16].

Solutions of the corresponding boundary value problems of the Poisson-Nernst-Planck-Stokes (PNPS) system are typically pursued numerically in two or three dimensions and often in a axially symmetric setting. However, as shown in Li and Muthukumar [19] the shape of a protein channel for example can be quite irregular and at the same time the specific geometry has a significant impact on the signaling in sequencing. Thus, even on the continuum level, parameter studies can be computationally time consuming.

Asymptotic analysis is a valuable tool for identifying the predominant physical mechanisms governing the system in specific regimes, such as high or low ion concentration, strong electric fields, confined geometries, etc.. The simplification of the full PNPS model can facilitate more profound analysis of the system's behavior as a function of specific parameters (e.g. ion concentration, electric potential, nanopore size, etc.). Consequently, significant insights into the limiting behavior of ion transport and electrostatics in nanopores under various conditions can be obtained. Thereby facilitating the derivation of scaling laws, the prediction of current-voltage characteristics, and the optimization of nanopore designs.

A variety of approaches exist for the reduction of model complexity. Ion channels typically have a small aspect ratio and this fact has been used to reduce the PNPS system by introducing area-averaged 1D models for axially symmetric cases, see for example [11, 27]. Similar ideas had also been pursued for the simpler PNP system by Singer et al. [32]. The underlying assumptions are that the variations of the concentrations and the electrostatic potential in the transverse and radial directions are negligible. Consequently, the averaged concentrations and potentials are calculated over the cross-sectional area of the channel. However, already for the PNP system strong radial variations of ion concentrations due to surface charges, for example, can not be captured with that approach as could be shown in Matejczyk et al. [22]. In fact, for the PNP model they showed that the assumption that the influence of the surface charge on the ion concentration and the voltage can be averaged over the cross section of the pore is only valid if the Debye length of the electrolyte is much larger than the pore width. In their analysis they present an asymptotic solution to the model for ion channels with radius comparable to the Debye length of the electrolyte. This asymptotic solution allows the characterization of the behavior of the ion channel in terms of the solution to a 1D model. By comparison to numerical solutions in their cas studies they demonstrate that the 1D area averaged PNP equations do not provide a good approximation to the full two-dimensional equations except for extremely dilute electrolytes or very narrow pores so that the Debye length of the electrolyte is much larger than the radius of the channel. Inspired by this study and the success of the long-wave approximation in thin liquid films [6] or in shallow water waves [38], we derive an asymptotic model for the axially symmetric boundary value problem for the PNPS system in the distinguished limit where the Debye length is comparable to the pore radius. It is in particular the limit where the charge selectivity is most pronounced [31].

In our analysis we first show convergence of the full two-dimensional axially symmetric problem to the quasi-1D asymptotic model. We then use our model to revisit a number of application problems in order to demonstrate the predictive potential of our model and discuss in the outlook several further extensions of the asymptotic model.

2 The Poisson-Nernst-Planck-Stokes system

We consider a system with two ion species, one anion $\tilde{c}_-$ and one cation $\tilde{c}_+$ and a viscous incompressible fluid. Furthermore, we consider an axially symmetric domain

$$\Omega = \left\{(\tilde{x}, \tilde{y}, \tilde{z}) : 0 \leq \tilde{z} \leq \tilde{L},\, 0 \leq \sqrt{\tilde{x}^2 + \tilde{y}^2} \leq \tilde{R}(\tilde{z})\right\},$$

such as given in Figure 1. The radius $\tilde{R}(\tilde{z})$ is a function of $\tilde{z}$. At $\tilde{z} = 0$ we prescribe an outlet boundary S^{out} and at $\tilde{z} = \tilde{L}$ an inlet boundary S^{in}. We denote the surface of the ion channel by S^{wall} and the symmetry axis at $\tilde{r} = \sqrt{\tilde{x}^2 + \tilde{y}^2} = 0$ by S^0.

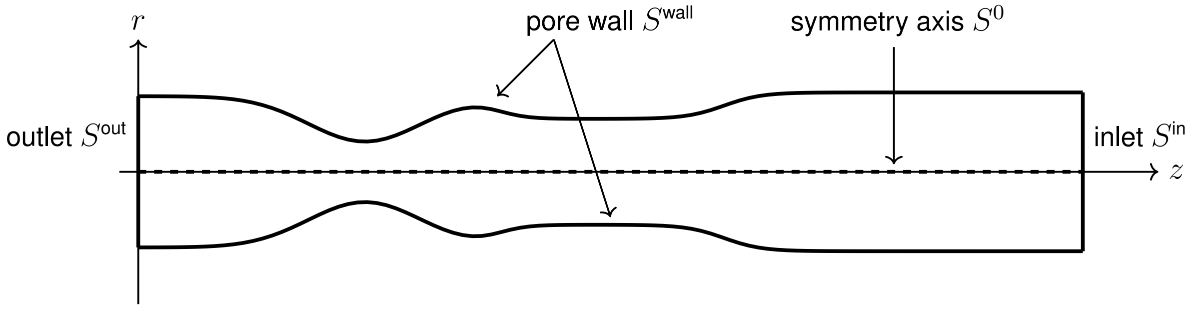

Figure 1: Sketch of an axially symmetric profile of an ion channel Ω. The pore wall at $r = R(z)$ is denoted with S^{wall}, the symmetry axis of the domain at $r = 0$ is marked as S^0. At $z = 0$ the pore has an outlet and at $z = L$ an inlet boundary.

The Nernst-Planck equations describe the evolution of the molar densities $\tilde{c}_+(\mathbf{x}, t)$ and $\tilde{c}_-(\mathbf{x}, t)$ with valences $z_+ = 1$ and $z_- = -1$ by

$$\partial_{\tilde{t}} \tilde{c}_\pm = -\tilde{\nabla} \cdot \tilde{\mathbf{J}}_\pm = -\tilde{\nabla} \cdot \left[\tilde{\mathbf{v}} \tilde{c}_\pm - \tilde{D}_\pm \left(\tilde{\nabla} \tilde{c}_\pm \pm \frac{F}{R_G T} \tilde{c}_\pm \tilde{\nabla} \tilde{\varphi}\right)\right], \tag{1}$$

with diffusion coefficients $\tilde{D}_\pm$, the molar gas constant R_G, the temperature T and the Faraday constant F. The electrostatic potential $\tilde{\varphi}(\mathbf{x}, t)$ is given by the Poisson equation

$$-\tilde{\nabla} \cdot (\varepsilon_0 (1 + \chi) \nabla \tilde{\varphi}) = F\left(\tilde{c}_+ - \tilde{c}_-\right), \tag{2}$$

with vacuum permittivity ε_0 and a constant dielectric susceptibility χ. Note that $\varepsilon_0(1+\chi) = \varepsilon_r$ is also often referred to as the relative permittivity. The above system is further coupled with the Stokes equations to calculate the velocity $\tilde{\mathbf{v}}(\mathbf{x}, t)$ and the pressure $\tilde{p}(\mathbf{x}, t)$. Which are given by the continuity equation

$$\tilde{\nabla} \cdot \tilde{\mathbf{v}} = 0 \tag{3}$$

and the momentum balance

$$-\nu\tilde{\Delta}\tilde{\mathbf{v}} + \tilde{\nabla}\tilde{p} = -F(\tilde{c}_+ - \tilde{c}_-)\tilde{\nabla}\tilde{\varphi}, \tag{4}$$

with viscosity ν. We apply Dirichlet boundary conditions for concentrations and potential on the outlet and inlet

$$\tilde{c}_\pm = \tilde{c}_\pm^{\text{out}},\ \tilde{\varphi} = \tilde{\varphi}^{\text{out}} \text{ on } S^{\text{out}} \text{ and } \tilde{c}_\pm = \tilde{c}_\pm^{\text{in}},\ \tilde{\varphi} = \tilde{\varphi}^{\text{in}} \text{ on } S^{\text{in}}, \tag{5a}$$

and normal stress boundary conditions for the velocity and the pressure

$$\nu\tilde{\nabla}\tilde{\mathbf{v}} \cdot \tilde{\mathbf{n}} - \tilde{p}\tilde{\mathbf{n}} = \tilde{p}^{\text{out}}\tilde{\mathbf{n}} \text{ on } S^{\text{out}},\ \nu\tilde{\nabla}\tilde{\mathbf{v}} \cdot \tilde{\mathbf{n}} - \tilde{p}\tilde{\mathbf{n}} = \tilde{p}^{\text{in}}\tilde{\mathbf{n}} \text{ on } S^{\text{in}}. \tag{5b}$$

On the channel wall we apply a constant surface charge

$$-\varepsilon_0(1+\chi)\tilde{\nabla}\tilde{\varphi} \cdot \tilde{\mathbf{n}} = \tilde{\sigma}(\tilde{z}) \text{ on } S^{\text{wall}}, \tag{5c}$$

a slip condition $\tilde{\mathbf{v}}_s$ for the velocity and no-flux boundary condition for the ion species

$$\tilde{b}\nabla\tilde{\mathbf{v}} \cdot \tilde{\mathbf{n}} = \tilde{\mathbf{v}}_s,\ \tilde{\mathbf{J}}_\pm \cdot \tilde{\mathbf{n}} = 0 \text{ on } S^{\text{wall}}. \tag{5d}$$

Furthermore, we define the following symmetry conditions at $\tilde{r} = 0$

$$\tilde{\mathbf{J}}_\pm \cdot \tilde{\mathbf{n}} = 0,\ \varepsilon_0(1+\chi)\tilde{\nabla}\tilde{\varphi} \cdot \tilde{\mathbf{n}} = 0,\ \nu\tilde{\nabla}\tilde{\mathbf{v}} \cdot \tilde{\mathbf{n}} - \tilde{p}\tilde{\mathbf{n}} = \mathbf{0} \text{ on } S^0. \tag{5e}$$

A crucial property of this system is the ionic current that flows through the pore. The current passing through surface S in z-direction can be calculated as follows

$$\tilde{I}_\pm = \pm F \int_S \tilde{\mathbf{J}}_\pm \cdot \tilde{\mathbf{n}}\, \mathrm{d}S, \tag{6}$$

with the total current

$$\tilde{I} = \tilde{I}_+ + \tilde{I}_-. \tag{7}$$

Scaled axially symmetric problem in the large-aspect-ratio limit. Since we consider a rotational symmetric problem we rewrite the system in cylindrical coordinates. The velocity field is given by $\tilde{\mathbf{v}} = (\tilde{w}, \tilde{u})$ where $\tilde{w}$ is the radial component and $\tilde{u}$ the axial component. Similar for the slip condition $\tilde{\mathbf{v}}_s = (\tilde{w}_s, \tilde{u}_s)$. For the large aspect ratio scaling we introduce a typical pore length $L_0 = 10^{-8} - 10^{-6}\,\mathrm{m}$ and a typical pore radius $R_0 = 10^{-9}\,\mathrm{m}$. In addition, we define a typical time scale $\tau = 10^{-9}\,\mathrm{s}$, a reference concentration $c^R = 1\,\mathrm{mol\,L^{-1}}$ and a reference charge $\sigma^R = 0.16\,\mathrm{C}$. We introduce the following dimensionless variables $\tilde{z} = L_0 z,\ \tilde{r} = R_0 r,\ \tilde{t} = \tau t,\ \tilde{D}_\pm = D^R k_\pm,\ \tilde{c}_\pm = c^R c_\pm,\ \tilde{\varphi} = \varphi^R \varphi,\ \tilde{u} = u^R u,\ \tilde{w} = \delta u^R w,\ \tilde{p} = p^R p\ \tilde{\sigma} = \sigma^R \sigma\ \tilde{b} = b^R b$. This gives us the ability to introduce the following dimensionless parameters

$$D^R = \frac{L_0^2}{\tau},\ \varphi^R = \frac{F}{R_G T},\ p^R = c^R RT,\ u^R = \frac{c^R R_G T\, R_0^2}{\nu L_0},\ I^R = \frac{F R_0^2 D^R c^R}{L_0},\ b^R = L_0 \tag{8a}$$

and

$$\Lambda^2 = \frac{\varepsilon_0(1+\chi)\varphi^R}{Fc^R R_0^2} = \frac{\lambda^2}{R_0^2},\ \gamma = \frac{R_0\sigma^R}{\varepsilon_0(1+\chi)\varphi^R},\ P_e = \frac{u^R L_0}{D^R},\ \delta = \frac{R_0}{L_0}. \tag{8b}$$

The scaled Nernst-Planck equations in cylindrical coordinates are given by

$$\delta^2\partial_t c_\pm = -\delta^2 P_e\left(w\partial_r c_\pm + u\partial_z c_\pm\right) + \delta^2\partial_z f_\pm + \frac{1}{r}\partial_r\left(rg_\pm\right), \tag{9a}$$

with the functions

$$f_\pm = k_\pm\left(\partial_z c_\pm \pm c_\pm\partial_z\varphi\right), \tag{9b}$$

and

$$g_\pm = k_\pm\left(\partial_r c_\pm \pm c_\pm\partial_r\varphi\right) \tag{9c}$$

for ease of notation. For the Poisson equation we find

$$-\delta^2\partial_{zz}\varphi - \frac{1}{r}\partial_r\left(r\partial_r\varphi\right) = \frac{1}{\Lambda^2}\left(c_+ - c_-\right). \tag{9d}$$

The dimensionless continuity equation in cylindrical coordinates yields

$$\frac{1}{r}\partial_r\left(rw\right) + \partial_z u = 0, \tag{9e}$$

and for the momentum balance we have

$$\delta^4\partial_{zz}w + \delta^2\left[\frac{1}{r}\partial_r\left(r\partial_r w\right) - \frac{1}{r^2}w\right] = \partial_r p + (c_+ - c_-)\partial_r\varphi, \tag{9f}$$

and

$$\delta^2\partial_{zz}u + \frac{1}{r}\partial_r\left(r\partial_r u\right) = \partial_z p + \left(c_+ - c_-\right)\partial_z\varphi. \tag{9g}$$

The scaled boundary conditions on the in- and outlet are

$$c_\pm = c_\pm^{\text{out}},\ \varphi = \varphi^{\text{out}} \text{ on } S^{\text{out}}, \text{ and } c_\pm = c_\pm^{\text{in}},\ \varphi = \varphi^{\text{in}} \text{ on } S^{\text{in}}, \tag{10a}$$

$$\delta^2\partial_z u - p = p^{\text{out}} \text{ on } S^{\text{out}}, \quad \delta^2\partial_z u - p = p^{\text{in}} \text{ on } S^{\text{in}}. \tag{10b}$$

On the channel wall we have

$$\partial_r\varphi - \delta^2 R'(z)\partial_z\varphi = -\sigma(z)\gamma\left(1 + \delta^2(R'(z))^2\right)^{1/2} \text{ on } S^{\text{wall}}, \tag{10c}$$

$$b\partial_r w = \delta w_s,\ b\partial_z u = u_s,\ \delta^2 R'(z)f_\pm - g_\pm = 0 \text{ on } S^{\text{wall}}, \tag{10d}$$

with the normal vector

$$\mathbf{n} = \left(\mathbf{e}_r - \delta R'(z)\mathbf{e}_z\right)\left(1 + \delta^2(R'(z))^2\right)^{-1/2},$$

where $\mathbf{e}_r$ is the normal vector in $r-$direction and $\mathbf{e}_z$ in $z-$direction,

$$\partial_r\varphi = 0,\ \delta^2\partial_r w - p = 0,\ \partial_r u = 0, \text{ on } S^0 \tag{10e}$$

and

$$-P_e\left(\delta^2 wc_\pm + \delta uc_\pm\right) + \delta f_\pm + g_\pm = 0 \text{ on } S^0. \tag{10f}$$

The current flowing through S at z-direction is given by the integral over the disk

$$I_\pm = \pm 2\pi\int_0^{R(z)}(P_e c_\pm u - f_\pm)r\,\mathrm{d}r. \tag{11}$$

3 Large aspect ratio asymptotics of the system

We use the following ansatz in order to find an asymptotic solution for the system in the limit of a very small aspect ratio $\delta \to 0$:

$$(c_\pm, \varphi, u, w, p) = (c_\pm^0 + \delta^2 c_\pm^1, \varphi^0 + \delta^2\varphi^1, u^0 + \delta^2 u^1, w^0 + \delta^2 w^1, \varphi^0 + \delta^2 p^1) + O(\delta^4) \quad (12)$$

In this study, the focus is on the case of the Debye length being equivalent or smaller to the radius of the pore, i.e., $\Lambda \le \mathcal{O}(1)$ and $\lambda \le \mathcal{O}(R_0)$. Additionally, we assume a substantial surface charge, characterized by the condition $\gamma = \mathcal{O}(1)$ and a large aspect ratio, denoted by $\delta \ll 1$.

Note that we calculate the asymptotic model for a system with no-slip boundary condition on S^{wall} for the velocity, such that $u|_{r=R(z)} = w|_{r=R(z)} = 0$.

Poisson equation. To leading order $\mathcal{O}(1)$, (9d) becomes

$$-\frac{1}{r}\partial_r\left(r\partial_r\varphi^0\right) = \frac{1}{\Lambda^2}\left(c_+^0 - c_-^0\right). \quad (13a)$$

Since c_+^0 and c_-^0 are functions of φ^0 this equation has to be solved later together with the leading order boundary conditions (from (10c) and (10e), respectively)

$$\partial_r\varphi^0|_{r=R(z)} = -\gamma\sigma(z), \quad \text{and} \quad \partial_r\varphi^0|_{r=0} = 0. \quad (13b)$$

The solution for φ^0 of this boundary value problem is not unique, since the homogeneous problem for φ^0 is satisfied by an arbitrary $\varphi_z^0(z)$. Therefore, if there is a particular solution of the inhomogeneous problem, say $\varphi_r^0(r,z)$, then any other solution can be achieved via

$$\varphi^0(r,z) = \varphi_r^0(r,z) + \varphi_z^0(z), \quad (14)$$

with an arbitrary $\varphi_z^0(z)$. Moreover, existence requires a solvability condition to be satisfied, which is obtained by simply integrating (13a) and using (13b). The result is the electroneutrality condition

$$\int_0^{R(z)} (c_+^0 - c_-^0) r dr - \Lambda^2\gamma\sigma R(z) \stackrel{!}{=} 0. \quad (15)$$

Notice that this condition includes the surface charges, so the net charge *in the fluid itself* must be negative inside the pipe. For the second order $\mathcal{O}(\delta^2)$ we find from equation (9d)

$$\frac{1}{r}\partial_r(r\partial_r\varphi^1) + \partial_z(\partial_z\varphi^0) = 0. \quad (16)$$

Integrating the equation with respect to r and using the boundary condition (from (10c) and (10e), respectively)

$$\partial_r\varphi^1|_{r=R(z)} - R'(z)\partial_z\varphi^0|_{r=R(z)} = 0 \quad \text{and} \quad \partial_r\varphi^1|_{r=0} = 0. \quad (17)$$

gives

$$0 = \int_0^{R(z)} \partial_r(r\partial_r\varphi^1)\,\mathrm{d}r + \int_0^{R(z)} \partial_z(\partial_z\varphi^0) r\,\mathrm{d}r = \partial_z \int_0^{R(z)} \partial_z\varphi_z^0 r\,\mathrm{d}r. \quad (18)$$

For a detailed computation see equation (66) in the appendix. This can now be used to fix expression for φ_z^0 in (14). Plugging that decomposition into the preceding identity yields

$$\varphi_z^0 = C_1 \int_0^z \frac{1}{R^2(z)}\,\mathrm{d}z + C_2. \tag{19}$$

Applying the boundary conditions (9a)

$$\varphi_z^0|_{z=L} = \varphi^{\text{in}},\ \varphi_r^0|_{z=L} = 0 \ \text{ and }\ \varphi_z^0|_{z=0} = \varphi^{\text{out}},\ \varphi_r^0|_{z=0} = 0, \tag{20}$$

allows us to determine the constants C_1 and C_2. We obtain

$$\varphi_z^0 = (\varphi^{\text{in}} - \varphi^{\text{out}})\frac{I_{\varphi_z}(z) - I_{\varphi_z}(0)}{I_{\varphi_z}(L) - I_{\varphi_z}(0)} + \varphi^{\text{out}}, \tag{21a}$$

with

$$I_{\varphi_z}(z) = \int_0^z \frac{1}{R^2(z)}\,\mathrm{d}z. \tag{21b}$$

Nernst-Planck equations In the leading order $\mathcal{O}(1)$ for the concentrations we have from (9a) and (9c)

$$\frac{1}{r}\partial_r\left(rg_\pm^0\right) = 0. \tag{22}$$

We integrate with respect to r gives together with the leading order of the third boundary condition in (71)

$$g_\pm^0 = \partial_r c_\pm^0 \pm c_\pm^0 \partial_r \varphi^0 = 0. \tag{23}$$

Using (14) for φ^0 we obtain

$$c_\pm^0 = Q_\pm(z,t)\mathrm{e}^{\mp\varphi_r^0} \tag{24}$$

with arbitrary $Q_\pm(z,t)$. Notice the leading order of (71) imposes the condition $g_\pm^0 = 0$, but this is automatically the case since φ^0 and hence φ_r^0 satisfies (13b). For the second order $\mathcal{O}(\delta^2)$ we obtain from equation (9a)

$$\partial_t c_\pm = -P_e\left(w^0\partial_r c_\pm^0 + u^0\partial_z c_\pm^0\right) + \partial_z f_\pm^0 + \frac{1}{r}\partial_r\left(rg_\pm^1\right). \tag{25}$$

In order to solve this equation we will introduce the stream function

$$s = \int_0^r u^0 r\,\mathrm{d}r, \tag{26}$$

such that $u^0 = r^{-1}\partial_r s$ and $w = -r^{-1}\partial_z s$. Integrating above equation gives together with the boundary condition $R'(z)f_\pm^0|_{r=R(z)} - g_\pm^1|_{r=R(z)} = 0$ the following result

$$\begin{aligned}\partial_t c_\pm &= -P_e\int_0^{R(z)}\left(-\partial_z s\partial_r c_\pm^0 + \partial_r s\partial_z c_\pm^0\right)\mathrm{d}r + \int_0^{R(z)}\partial_z f_\pm^0 r\,\mathrm{d}r + \int_0^{R(z)}\partial_r\left(rg_\pm^1\right)\mathrm{d}r \\ &= P_e\partial_z\int_0^{R(z)} c_\pm^0 u^0 r\,\mathrm{d}r + k_\pm\partial_z\int_0^{R(z)}\left(\partial_z c_\pm^0 \pm c_\pm^0\partial_z\varphi^0\right) r\,\mathrm{d}r.\end{aligned} \tag{27}$$

For a detailed calculation see equation (70) in the appendix. Using solution (24) and the ansatz (14) further gives

$$\partial_t Q_\pm \mathrm{e}^{\mp\varphi_r^0} = \partial_z \Bigg[P_e Q_\pm \int_0^{R(z)} \mathrm{e}^{\mp\varphi_r^0} u^0 r \,\mathrm{d}r \tag{28}$$

$$\pm k_\pm Q_\pm \int_0^{R(z)} (\partial_z \varphi_z^0) \mathrm{e}^{\mp\varphi_r^0} r \,\mathrm{d}r + k_\pm \partial_z Q_\pm \int_0^{R(z)} \mathrm{e}^{\mp\varphi_r^0} r \,\mathrm{d}r \Bigg].$$

This equation needs to be solved for $Q_\pm$ together with the boundary conditions (10a)

$$Q_\pm|_{z=L} = c_\pm^{\text{in}} \text{ and } Q_\pm|_{z=0} = c_\pm^{\text{out}}. \tag{29}$$

Momentum balance for no-slip. We can obtain a solution for the pressure from the leading order $\mathcal{O}(1)$ from equation (9f)

$$\partial_r p^0 = -(c_+^0 - c_-^0)\partial_r \varphi^0. \tag{30}$$

With a similar argumentation as for the potential we use the following ansatz for the pressure

$$p^0(r,z) = p_z^0(z) + p_r^0(r,z). \tag{31}$$

Using solution (24), integrating with respect to r yields together with the symmetry condition (10e) $p_r^0|_{r=0} = 0$

$$p_r^0 = Q_+ \left(\mathrm{e}^{-\varphi_r^0} - \mathrm{e}^{-\varphi_r^0|_{r=0}} \right) + Q_- \left(\mathrm{e}^{\varphi_r^0} - \mathrm{e}^{\varphi_r^0|_{r=0}} \right). \tag{32}$$

From equation (9g) we can derive a solution for the axial component of the velocity u^0

$$\frac{1}{r}\partial_r(r\partial_r u^0) = \partial_z p^0 + (c_+ - c_-)\partial_z \varphi^0. \tag{33}$$

We rewrite the derivatives of the pressure and the potential as follows

$$\partial_z p^0 = \partial_z p_z^0 + \partial_z p_r^0 = \Pi_z(z) + \Pi_r(r,z) \tag{34a}$$

and

$$\partial_z \varphi^0(r,z) = \partial_z \varphi_z^0 + \partial_z \varphi_r^0 = \mathsf{E}_z(z) + \mathsf{E}_r(r,z). \tag{34b}$$

Using equation (13a) we find

$$\frac{1}{r}\partial_r(r\partial_r u^0) = \Pi_z + \Pi_r - \Lambda^2(\mathsf{E}_z + \mathsf{E}_r)\frac{1}{r}\partial_r(r\partial_r \varphi_r^0). \tag{35}$$

Integrating with respect to r gives

$$r\partial_r u^0 = \Pi_z \frac{1}{2} r^2 + K_1(r,z) - \mathsf{E}_z \Lambda^2 r \partial_r \varphi^0 + h_1, \tag{36a}$$

with

$$K_1(r,z) = \int_0^r (\Pi_r r - \Lambda^2 \mathsf{E}_r \partial_r(r\partial_r \varphi_r^0))\,\mathrm{d}r. \tag{36b}$$

We can further rewrite K_1 by using equation (13a) to get

$$\begin{aligned} K_1(r,z) &= \int_0^r (\Pi_r r - \Lambda^2 \mathsf{E}_r \partial_r (r \partial_r \varphi_r^0))\, \mathrm{d}r \\ &= \int_0^r (\partial_z p_r^0 + \partial_z \varphi_r^0 (Q_+ \mathrm{e}^{-\varphi_r^0} - Q_- \mathrm{e}^{\varphi_r^0})) r\, \mathrm{d}r \\ &= \int_0^r \Big(\partial_z Q_+ (\mathrm{e}^{-\varphi_r^0} - \mathrm{e}^{-\varphi_r^0|_{r=0}}) + \partial_z Q_- (\mathrm{e}^{\varphi_r^0} - \mathrm{e}^{\varphi_r^0|_{r=0}}) \\ &\qquad + \partial_z (\varphi_r^0|_{r=0})(Q_+ \mathrm{e}^{-\varphi_r^0|_{r=0}} - Q_- \mathrm{e}^{\varphi_r^0|_{r=0}}) \Big)\, r\, \mathrm{d}r. \end{aligned} \tag{37}$$

With the symmetry condition (10e) at $r = 0$ we find $\partial_r u^0|_{r=0} = r^{-1}(h_1 + K_1(r = 0, z)) = 0$ and hence $h_1 \overset{!}{=} -K_1(r = 0, z)$. Note that the integrand of K_1 is the equilibrium between the axial gradient of the electric double layer (EDL) pressure and the axial electrostatic force. density. Integrating again with respect to r gives

$$u^0 = \Pi_z \frac{1}{4} r^2 + K_2(r,z) - \mathsf{E}_z \Lambda^2 \varphi^0 + h_2, \tag{38a}$$

with

$$K_2(r,z) = \int_0^r \frac{1}{r} (K_1(r,z) - K_1(r = 0, z))\, \mathrm{d}r. \tag{38b}$$

Note that K_2 is an EDL-driven axial flow contribution. Together with the no-slip condition (9d) $u^0|_{r=R(z)} = 0$, we get

$$u^0 = \Pi_z \frac{1}{4} \left(r^2 - R^2(z)\right) + K_2(r,z) - K_2(r = R(z), z) - \mathsf{E}_z \Lambda^2 \zeta(r,z), \tag{39a}$$

with the $\zeta-$potential

$$\zeta = \varphi_r^0 - \varphi_r^0|_{r=R(z)}, \tag{39b}$$

Continuity equation for no-slip. We need to ensure that the continuity equation (9e) is fulfilled. Therefore, we integrate the leading order $\mathcal{O}(1)$ with respect to r from 0 to $R(z)$ which gives

$$\begin{aligned} 0 &= \int_0^{R(z)} \left(\partial_r (r w^0) + (\partial_z u^0) r \right)\, \mathrm{d}r \\ &= R(z) \underbrace{\left(w^0|_{r=R(z)} - R'(z) u^0|_{r=R(z)} \right)}_{=0} + \partial_z \int_0^{R(z)} u^0 r\, \mathrm{d}r. \end{aligned} \tag{40}$$

Together with no-slip $w^0|_{r=R(z)} = u^0|_{r=R(z)} = 0$ and the solution (39a) for u^0 we have

$$\partial_z \left[\Pi_z \frac{1}{4} \int_0^{R(z)} \left(r^2 - R^2(z)\right) r\, \mathrm{d}r + K_3(z) - \mathsf{E}_z \Lambda^2 \int_0^{R(z)} \zeta\, r\, \mathrm{d}r \right] = 0, \tag{41a}$$

with

$$K_3(z) = \int_0^{R(z)} (K_2(r,z) - K_2(r = 0, z)) r\, \mathrm{d}r. \tag{41b}$$

Solving this equation gives

$$p_z^0 = C_2 + C_1 I_p(z) - \int_0^z \left(\frac{16\Lambda^2 \mathsf{E}_z}{R^4(z)} \int_0^{R(z)} \zeta \, r \, \mathrm{d}r \right) \mathrm{d}z + \int_0^z \frac{16 K_3(z)}{R^4(z)} \, \mathrm{d}z, \tag{42a}$$

with

$$I_p(z) = \int_0^{R(z)} \frac{1}{R^4(z)} \, \mathrm{d}z \tag{42b}$$

with the boundary conditions (10b)

$$p_z^0|_{z=0} = -p^{\text{out}}, \; p_r^0|_{z=0} = 0 \; \text{ and } \; p_z^0|_{z=L} = -p^{\text{in}}, \; p_r^0|_{z=L} = 0, \tag{43}$$

the following solution

$$p_z^0 = -(p^{\text{in}} - p^{\text{out}}) \frac{I_p(z) - I_p(z=0)}{I_p(z=L) - I_p(z=0)} - p^{\text{out}} - \Psi(z) + K_4(z), \tag{44a}$$

with

$$\Psi(z) = I_{\mathsf{E}_z}(z) - I_{\mathsf{E}_z}(z=0) - \frac{I_{\mathsf{E}_z}(z=L) - I_{\mathsf{E}_z}(z=0)}{I_p(z=L) - I_p(z=0)} \left(I_p(z) - I_p(z=0) \right) \tag{44b}$$

$$I_{\mathsf{E}_z}(z) = \int_0^z \left(\frac{16\Lambda^2 \mathsf{E}_z}{R^4(z)} \int_0^{R(z)} \left[\varphi_r^0 - \varphi_r^0|_{r=R(z)} \right] r \, \mathrm{d}r \right) \mathrm{d}z, \tag{44c}$$

$$K_4(z) = I_{K_3}(z) - I_{K_3}(z=0) - \frac{I_{K_3}(z=L) - I_{K_3}(z=0)}{I_p(z=L) - I_p(z=0)} \left(I_p(z) - I_p(z=0) \right) \tag{44d}$$

and

$$I_{K_3}(z) = \int_0^z \frac{16}{R^4(z)} K_3(z) \, \mathrm{d}z. \tag{44e}$$

Current. The leading order $\mathcal{O}(1)$ currents are calculated as follows

$$I_\pm = \pm k_\pm \left(\partial_z Q_\pm \pm Q_\pm \mathsf{E}_z \right) \int_0^{R(z)} \mathrm{e}^{\mp \varphi_r^0} \, r \, \mathrm{d}r \pm P_e Q_\pm \int_0^{R(z)} u^0 \mathrm{e}^{\mp \varphi_r^0} \, r \, \mathrm{d}r. \tag{45}$$

4 The asymptotic model

In order to get the solutions for $\varphi_r^0(r,z)$ and $Q_\pm(z)$ we have to solve the following three coupled 1D ordinary differential equations (ODEs) numerically. The pseudocode is given in the appendix by Algorithm 1. In the r-direction we have to solve

$$-\frac{1}{r} \partial_r (r \partial_r \varphi_r^0) = \frac{1}{\Lambda^2} (Q_+ \mathrm{e}^{-\varphi_r^0} - Q_- \mathrm{e}^{\varphi_r^0}), \tag{46a}$$

with the boundary conditions

$$\partial_r \varphi_r^0|_{r=R(z)} = -\gamma\sigma(z), \quad \text{and} \quad \partial_r \varphi_r^0|_{r=0} = 0 \tag{46b}$$

for every point in z. In $z-$direction we have to calculate

$$\partial_t Q_\pm \mathrm{e}^{\mp\varphi_r^0} = \partial_z \left[k_\pm(\partial_z Q_\pm) H_1(\varphi_r^0) \pm k_\pm Q_\pm H_2(\varphi_r^0, \varphi_z^0) - P_e Q_\pm H_3(\varphi_r^0, u^0)\right] \tag{47a}$$

for every timestep in t, with

$$H_1 = \int_0^{R(z)} \mathrm{e}^{\mp\varphi_r^0}\, r\,\mathrm{d}r, \quad H_2 = \int_0^{R(z)} (\partial_z \varphi_z^0)\mathrm{e}^{\mp\varphi_r^0}\, r\,\mathrm{d}r, \quad H_3 = \int_0^{R(z)} u^0 \mathrm{e}^{\mp\varphi_r^0}\, r\,\mathrm{d}r \tag{47b}$$

and the boundary conditions

$$Q_\pm|_{z=0} = c_\pm^{\text{out}}, \quad \text{and} \quad Q_\pm|_{z=L} = c_\pm^{\text{in}}. \tag{47c}$$

From that we can calculate the concentrations with

$$c_\pm^0(r,z) = Q_\pm \mathrm{e}^{\mp\varphi_r^0}, \tag{48}$$

and the total electrostatic potential

$$\varphi^0(r,z) = \varphi_r^0(r,z) + \varphi_z^0(z), \tag{49a}$$

with

$$\varphi_z^0(z) = (\varphi^{\text{in}} - \varphi^{\text{out}})\Delta I_{\varphi_z} + \varphi^{\text{out}}, \tag{49b}$$

and

$$\Delta I_{\varphi_z} = \frac{I_{\varphi_z}(z) - I_{\varphi_z}(0)}{I_{\varphi_z}(z=L) - I_{\varphi_z}(z=0)} \quad \text{and} \quad I_{\varphi_z} = \int_0^z \frac{1}{R^2(z)}\,\mathrm{d}z. \tag{49c}$$

Note that for $R(z) = R =$const. we get $\Delta I_{\varphi_z} = z/L$. The total pressure is given by

$$p^0(r,z) = p_r^0(r,z) + p_z^0(z), \tag{50a}$$

with

$$p_r^0(r,z) = Q_+\left(\mathrm{e}^{-\varphi_r^0} - \mathrm{e}^{-\varphi_r^0|_{r=0}}\right) + Q_-\left(\mathrm{e}^{\varphi_r^0} - \mathrm{e}^{\varphi_r^0|_{r=0}}\right) \tag{50b}$$

and

$$p_z^0(z) = -(p^{\text{in}} - p^{\text{out}})\Delta I_p(z) - p^{\text{out}} - \Psi(z) + K_4(z), \tag{50c}$$

with

$$\Delta I_p = \frac{I_p(z) - I_p(z=0)}{I_p(z=L) - I_p(z=0)} \quad \text{and} \quad I_p(z) = \int_0^z \frac{1}{R^4(z)}\,\mathrm{d}z, \tag{50d}$$

such that for $R(z) = R =$const. we get $\Delta I_p = z/L$,

$$\Psi(z) = I_{\mathsf{E}_z}(z) - I_{\mathsf{E}_z}(z=0) - (I_{\mathsf{E}_z}(z=L) - I_{\mathsf{E}_z}(z=0))\Delta I_p(z), \tag{50e}$$

$$K_4(z) = I_{K_3}(z) - I_{K_3}(z=0) - (I_{K_3}(z=L) - I_{K_3}(z=0))\Delta I_p(z) \tag{50f}$$

and

$$I_{\mathsf{E}_z}(z) = \int_0^z \left(\frac{16\Lambda^2(\partial_z \varphi_z^0)}{R^4(z)} \int_0^{R(z)} \zeta \, r \, \mathsf{d}r \right) \mathsf{d}z \quad \text{and} \quad I_{K_3}(z) = \int_0^z \frac{16}{R^4(z)} K_3(z) \, \mathsf{d}z, \tag{50g}$$

where

$$\zeta = \varphi_r^0 - \varphi_r^0|_{r=R(z)}, \tag{50h}$$

$$K_3(z) = \int_0^{R(z)} (K_2(r,z) - K_2(r=0,z)) r \, \mathsf{d}r, \tag{50i}$$

$$K_2(r,z) = \int_0^r \frac{1}{r}(K_1(r,z) - K_1(r=0,z)) \, \mathsf{d}r \tag{50j}$$

and

$$K_1(r,z) = \int_0^r \Big(\partial_z Q_+ (\mathsf{e}^{-\varphi_r^0} - \mathsf{e}^{-\varphi_r^0|_{r=0}}) + \partial_z Q_- (\mathsf{e}^{\varphi_r^0} - \mathsf{e}^{\varphi_r^0|_{r=0}}) \\ + \partial_z(\varphi_r^0|_{r=0})(Q_+ \mathsf{e}^{-\varphi_r^0|_{r=0}} - Q_- \mathsf{e}^{\varphi_r^0|_{r=0}}) \Big) \, r \, \mathsf{d}r. \tag{50k}$$

The velocity is then calculated as

$$u^0(r,z) = (\partial_z p_z^0)\frac{1}{4}\left(r^2 - R^2(z)\right) - (\partial_z \varphi_z^0)\Lambda^2 \zeta(r,z) + K_2(r,z) - K_2(r=R(z),z), \tag{51a}$$

with

$$\partial_z p_z^0 = -\,(p^{\mathsf{in}} - p^{\mathsf{out}})\partial_z(\Delta I_p(z)) - \partial_z \Psi(z) + \partial_z K_4(z) \tag{51b}$$

and

$$\partial_z \varphi_z^0 = (\varphi^{\mathsf{in}} - \varphi^{\mathsf{out}})\partial_z(\Delta I_{\varphi_z}(z)). \tag{51c}$$

For the currents we have

$$I_\pm = k_\pm \left(\partial_z Q_\pm \pm Q_\pm \mathsf{E}_z \right) \int_0^{R(z)} \mathsf{e}^{\mp\varphi_r^0} \, r \, \mathsf{d}r \mp P_e Q_\pm \int_0^{R(z)} u^0 \mathsf{e}^{\mp\varphi_r^0} \, r \, \mathsf{d}r, \tag{52a}$$

with the total current given by

$$I = I_+ + I_-. \tag{52b}$$

5 Predictions of the asymptotic model

In this section we illustrate the wide spectrum of applications of our model for typical scenarios in nanotechnological and biological applications.

5.1 Electro-osmotic flow transitions arising in cylindrical nanopores

In order to better understand ion transport through nanopores, whether for improving existing technologies or developing new therapies, it is crucial to identify the driving forces behind EOF and understand how these change when, for example, an additional hydrodynamic pressure gradient is applied. In this example we will study a cylindrical pore with constant radius $R(z) = R$. When studying a straight pipe, we can ensure that no additional effects due to geometry play a role. As we saw in the previous example, adding a constriction leads to an additional pressure drop. This means that in a straight pipe, the influence of an applied pressure difference can be considered in isolation, whereas in a trumpet-shaped pore, for example, it is not clear what additional effects may occur. In addition, some of the equations in the asymptotic model for a cylindrical pore can be simplified. Therefore, we study a cylindrical pore with constant radius $R(z) = R = 5$ and a length of $L = 25$ with $\delta = 0.1$. As surface charge we define (62) with $q = 0.15$, $L_1 = 0.2L$, $L_2 = L - L_1$ and $\varepsilon = 5$. All other parameter values are given in Table 1 and Table 3.

5.1.1 Transitions in the flow regime

We calculated the volumetric flow $\langle u^0 \rangle = \int_0^L \int_0^R u^0 r \,\mathrm{d}r\, \mathrm{d}z$ in the pore for different salt concentrations $c_\pm^{\text{in}} = c_\pm^{\text{out}} = c^{\text{bulk}}$ (Figure 2), applied pressure differences $\Delta p = p^{\text{in}} - p^{\text{out}}$ and potential differences $\Delta\varphi = \varphi^{\text{in}} - \varphi^{\text{out}}$ between in- and outlet (Figure 3). If we integrate equation (39a) we get

$$\langle u^0 \rangle = \langle u^{\text{PF}} \rangle + \langle u^{\text{HS}} \rangle + \langle u^{\text{EDL}} \rangle = \Delta p \frac{1}{16} R^4 - \Lambda^2 \frac{\Delta\varphi}{L} \langle \zeta \rangle + \langle u^{\text{EDL}} \rangle. \tag{53}$$

As illustrated by Figure 3a the flow can be distinguished between two known regimes: a pressure-controlled regime characterized by a Poiseuille-like profile (PF)

$$\langle u^{\text{PF}} \rangle = \Delta p \frac{1}{16} R^4 \tag{54}$$

and a potential-driven (EOF) regime. The later is characterized by a Helmholtz-Smoluchowski-like profile (HS) [25], also referred to as electroosmotic velocity

$$\langle u^{\text{HS}} \rangle = -\Lambda^2 \frac{\Delta\varphi}{L} \langle \zeta \rangle, \tag{55}$$

where $\zeta = \varphi_r^0 - \varphi_r^0|_{r=R}$ is the zeta-potential. Additionally, a third term $\langle u^{\text{EDL}} \rangle$ with

$$\langle u^{\text{EDL}} \rangle = \int_0^L \int_0^R (K_2(r,z) - K_2(r=R,z)) r \,\mathrm{d}r\, \mathrm{d}z \tag{56}$$

plays a role as shown in Figure 2a. The function K_2 is give by equation (50j) and is a flow contribution arising from the EDL axial force density. Thus, the $\langle u^{\text{EDL}} \rangle$ gives us a correction for the flow due to large Debye length, i.e. for low concentrations with weak screening of the surface charge. For a detailed computation see Appendix B. However, we find that for a salt concentration high enough the EDL–term does not contribute significantly as illustrated in Figure 2a. For this example we did not apply a pressure difference, i.e. $\Delta p = 0$, such that $\langle u^{\text{PF}} \rangle = 0$. We then calculated the volumetric flow for different salt concentrations c^{bulk} and applied potential differences. It can be observed that for all $\Delta\varphi$, the flow initially increases with increasing concentration until a maximum is reached, and then decreases again. The maximum varies for the different potentials. In addition, we see that after the peak the flow follows the Helmholtz-Smoluchowski-like profile (dashed lines). Note that the zeta-potential $\langle \zeta \rangle$ also depends on the concentrations. For small concentrations we find that $\langle u^{\text{HS}} \rangle$ is almost constant and that the volumetric flow is driven by the sum of the HS–term and the EDL–term. If we scale flow with $\Delta\varphi$ it can be observed that for all potentials the maxima become equal. However, we still notice a rightward (or leftward) shift of the curves for small concentrations (Figure 2b).

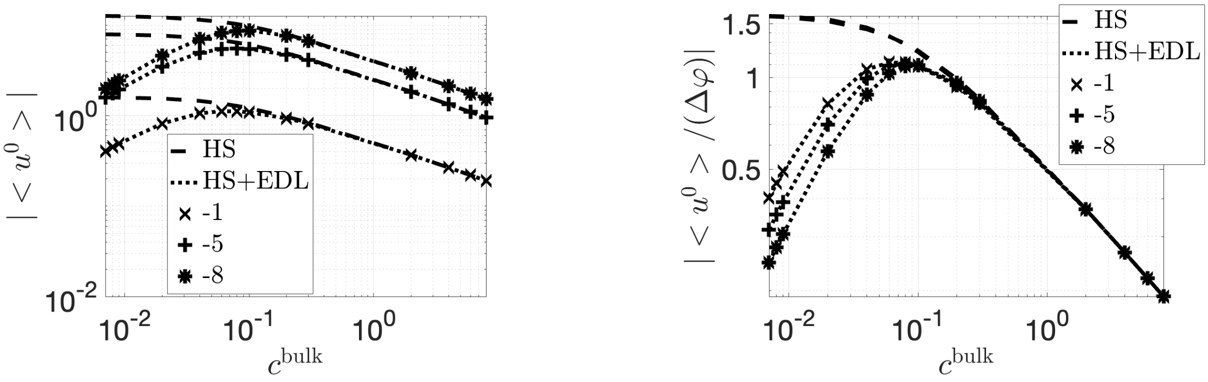

(a) (b)

Figure 2: (a) Volumetric flow $\langle u^0 \rangle$ plotted as a function of the bulk concentration c^{bulk} for $\Delta p = 0$ and different potentials $\Delta\varphi = -1$ (crosses), $\Delta\varphi = -5$ (plus signs) and $\Delta\varphi = -8$ (stars). The dashed line corresponds to the $\langle u^{\mathrm{HS}} \rangle$ (Helmholtz-Smoluchowski) flow regime. The dotted line gives $\langle u^{\mathrm{HS}} \rangle + \langle u^{\mathrm{EDL}} \rangle$. (b) Volumetric flow scaled with $\Delta\varphi$.

For the following study we chose the concentrations $c_\pm^{\mathrm{out}} = c_\pm^{\mathrm{in}} = c^{\mathrm{bulk}} = 0.6$ such that $\langle u^{\mathrm{EDL}} \rangle \ll \langle u^{\mathrm{HS}} \rangle$ (see Figure 2b) and the flow is given by $\langle u^0 \rangle = \langle u^{\mathrm{PF}} \rangle + \langle u^{\mathrm{HS}} \rangle$. We then calculated the volumetric flow for different applied pressure and potential differences to study the transition between the pressure-controlled and the potential-controlled regimes. We find that if we apply no potential difference ($\Delta\varphi = 0$) that the volumetric flow depends linearly on the pressure difference Δp (Figure 3a dotted line). On the other hand, if we apply zero pressure, we find that the velocity profile is constant which is illustrated in Figure 3a (dashed lines). Furthermore, we find for $\langle u^0 \rangle = 0$ that $\Delta p - C_u \langle \zeta \rangle \Delta\varphi = 0$, with $C_u = \Lambda^2 16/(R^4 L)$, such that

$$\langle u^0 \rangle \begin{cases} \leq 0 & \text{if } \Delta p \leq C_u \langle \zeta \rangle \Delta\varphi \quad \text{for } \langle \zeta \rangle \Delta\varphi \geq 0 \\ \geq 0 & \text{if } \Delta p \geq C_u \langle \zeta \rangle \Delta\varphi \quad \text{for } \langle \zeta \rangle \Delta\varphi \geq 0 \\ \geq 0 & \forall \Delta p \qquad\qquad\qquad\; \text{for } \langle \zeta \rangle \Delta\varphi \leq 0. \end{cases} \tag{57}$$

Depending on the sign of the applied potential and pressure difference as well as on the sign of the zeta-potential the volumetric flow changes its sign. For our example we calculated $\langle \zeta \rangle = -88$ and $C_u = 1.8e-4$ for all applied potential differences. As illustrated in Figure 3a we find that for negative potentials the absolute value of the flow first decreases with increasing pressure until a minimum is reached and then starts to increase again for increasing pressure. The minimum indicates the change in sign as shown in Figure 3b. For $\Delta\varphi = -0.2$ the change in sign is at $\Delta p = 0.0032$ (stars) and for $\Delta\varphi = -8$ the change in sign is at $\Delta p = 0.13$ (circles). For $\Delta\varphi = 0.2$ (crosses) and $\Delta\varphi = 8$ (plus signs), on the other hand, the flow rate increases steadily as the pressure increases.

Figure 3b shows the volumetric flow scaled by a factor of $C_u \langle \zeta \rangle \Delta\varphi$. While the unscaled data show clear quantitative differences between the applied potentials, rescaling the velocities by a factor of $C_u \langle \zeta \rangle \Delta\varphi$ results in a clear, uniform behavior. When plotted as normalized flow, all curves for negative potentials converge to a single master curve still reflecting the change in sign in the flow. Similarly, all curves for positive potentials merge into a single curve. This convergence suggests that the influence

DOI 10.20347/WIAS.PREPRINT.3243

of the potential difference can be incorporated into this scaling relationship, indicating universal transport behavior once the appropriate dimensionless scale is applied. This rescaling therefore provides a robust way to compare results across different potential landscapes and highlights the underlying physical mechanism that controls the flow. Furthermore, as illustrated in Figure 3b the flow is dominated by the HS regime for low pressure values until it continuously transitions into the PF regime for increasing pressure.

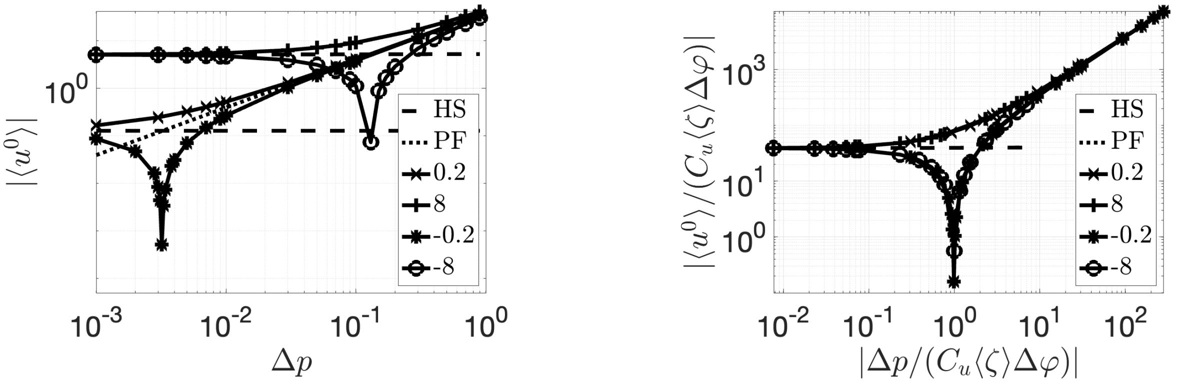

(a) (b)

Figure 3: (a) Volumetric flow $\langle u^0\rangle$ for $c^{\text{bulk}} = 0.6$ plotted as a function of pressure Δp for different potentials $\Delta\varphi = 0.2$ (crosses), $\Delta\varphi = 8$ (plus signs), $\Delta\varphi = -0.2$ (stars) and $\Delta\varphi = -8$ (circles). The dotted and dashed lines correspond to the $\langle u^{\text{PF}}\rangle$ (Poiseuille) and $\langle u^{\text{HS}}\rangle$ (Helmholtz-Smoluchowski) flow regimes, respectively. (b) Volumetric flow and pressure scaled with $C_u\Delta\varphi$.

We were able to show that, even though we use a general derivation for the asymptotic model without further simplifications such as small Debye length or a constant electric field (as in [25]), we can reconstruct two known solutions for the volumetric flow: Poiseuille and Helmholtz-Smoluchowski. While most studies only consider one of these two regimes, we show that the volumetric flow changes between them depending on the applied voltage and pressure differences. Moreover, our model shows that for small salt concentrations there is an additional contribution to the volumetric flow. Note that although the dependence of the flow on Δp and $\Delta\varphi$ is evident from equation (53), the zeta-potential still has to be calculated numerically. Since we observe in our numerical simulations that it does not change dramatically for different potentials and pressures, it only needs to be calculated once for a specific salt concentration and surface charge.

5.1.2 Transitions in the ion current

We also calculated the concentration and pressure dependency of the ionic currents flowing through a circular area at $z = 0$. Taking a closer look on equation (60) we find that the currents can be approximated as follows

$$\begin{aligned} I_\pm &= 2\pi c_\pm^{\text{bulk}} \left[\frac{\Delta\varphi}{L} \left(\frac{k_\pm}{2} R^2 + P_e \Lambda^2 \frac{\langle\zeta\rangle}{L} \right) \mp P_e \frac{\Delta p}{L} \frac{1}{16} R^4 \right] \\ &\quad \pm 2\pi k_\pm \frac{1}{2} R^2 \partial_z Q_\pm|_{z=0} \mp 2\pi c_\pm^{\text{bulk}} P_e \frac{\langle u^{\text{EDL}}\rangle}{L} \\ &= I_\pm^{\text{E}} + I_\pm^{\text{P}} + I_\pm^{\text{C}}, \end{aligned} \tag{58}$$

with $c_\pm^{\text{out}} = c_\pm^{\text{in}} = c_\pm^{\text{bulk}}$. A detailed computation can be found in the Appendix 60. Overall, the current can be written as the sum of a potential-driven (EOF) current I^{E}, a pressure-driven current I^{P} and a third concentration-dependent term I^{C} giving us a large Debye layer-correction for the current. Similar as for the volumetric flow we now find that I^{C}–term only plays a role for small concentrations when the Debye layer is large (see Figure 4). For all three applied voltages $\Delta\varphi = -1$ (crosses), $\Delta\varphi = -5$ (plus signs) and $\Delta\varphi = -8$ (stars), the measured current rise continuously with increasing concentrations (Figure 4a).

Scaling the current with $\Delta\varphi$ as given in Figure 4b shows that in all three cases the current continuously transitions into the I^{E}–curve (dashed line) indicating that the potential-driven regime dominates there. Note that $I/\Delta\varphi$ is often also reffered to as conductance. For small concentrations it can be observed that the I^{C}-term is negligible. Furthermore, we find that with that scaling all three curves collapse into one curve for high salt concentrations while there is still a slight rightward (or leftward) shift for small concentrations. At sufficiently high concentrations, we therefore find that the current consists of a pressure-driven and a potential-driven regime.

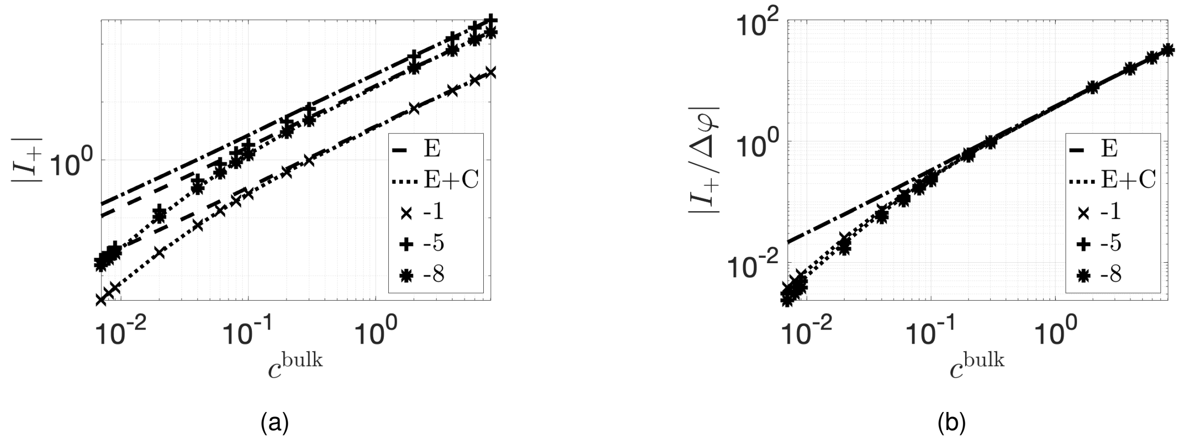

Figure 4: (a) Cation current I_+ plotted as a function of the bulk concentration c^{bulk} for $\Delta p = 0$ and different potentials $\Delta\varphi = -1$ (crosses), $\Delta\varphi = -5$ (plus signs) and $\Delta\varphi = -8$ (stars). The dashed line corresponds to the I^{E} (potential-driven) regime. The dotted line gives $I^{\text{E}} + I^{\text{C}}$. (b) Cation current scaled with $c^{\text{bulk}}\Delta\varphi$.

For concentrations where $I_\pm^{\text{C}} \ll I_\pm^{\text{E}}$ (see Figure 4b) it can additionally be observed that there is a switch in the sign of the cation current depending on the applied potential and pressure. For $I_\pm = 0$ we have $\Delta p \mp C_\pm \Delta\varphi = 0$, with $C_\pm = k_+ 8/(P_e R^2) + \Lambda^2 \langle\zeta\rangle 16/(LR^4)$, such that

$$I_+ \begin{cases} \leq 0 & \text{if } \Delta p \leq C_+\Delta\varphi \quad \text{for } C_+\Delta\varphi \geq 0 \\ \geq 0 & \text{if } \Delta p \geq C_+\Delta\varphi \quad \text{for } C_+\Delta\varphi \geq 0 \\ \geq 0 & \forall \Delta p \qquad\qquad\quad \text{for } C_+\Delta\varphi \leq 0 \end{cases} \tag{59}$$

and

$$I_- \begin{cases} \leq 0 & \text{if } \Delta p \leq C_-\Delta\varphi \quad \text{for } C_-\Delta\varphi \leq 0 \\ \geq 0 & \text{if } \Delta p \geq C_-\Delta\varphi \quad \text{for } C_-\Delta\varphi \leq 0 \\ \geq 0 & \forall \Delta p \qquad\qquad\quad \text{for } C_-\Delta\varphi \geq 0. \end{cases} \tag{60}$$

We calculated the absolute cation current for $c^{\text{bulk}} = 0.6$ as a function of Δp for different potential differences $\Delta\varphi = 1$, $\Delta\varphi = 2$ and $\Delta\varphi = -1$ (Figure 5a). For this example we calculate $\langle\zeta\rangle =$

-88 and $C_+ = 0.14$. For positive potentials it can be observed, as illustrated in Figure 5b, that for increasing pressure, the cation current first decreases, reaches a minimum, and then increases. The respective change in sign here is at approximately $\Delta p = 0.14$ (for $\Delta\varphi = 1$) and $\Delta p = 0.28$ (for $\Delta\varphi = 2$) (Figure 5a). For $\Delta\varphi = -1$, however, we do not observe any reversal of the current. In this case, the current increases continuously with increasing pressure.

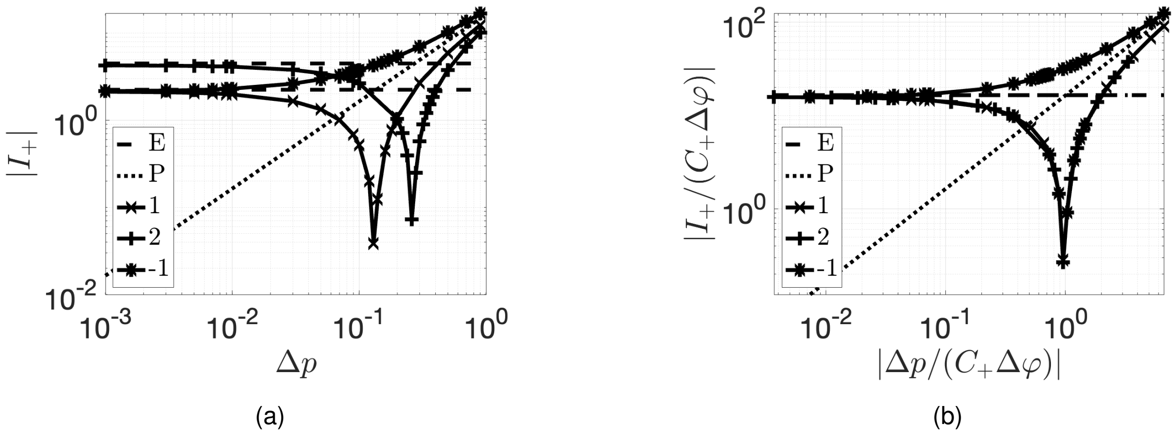

Figure 5: (a) Cation current I_+ for $c^{\text{bulk}} = 0.6$ plotted as a function of pressure Δp for different potentials $\Delta\varphi = 1$ (crosses), $\Delta\varphi = 2$ (plus signs), $\Delta\varphi = -1$ (stars). The dotted and dashed lines correspond to the I^{P} (pressure-driven) and I^{E} (potential-driven) current regimes, respectively. (b) Current and pressure scaled with $C_+\Delta\varphi$.

Similar to the flow, we find that when the current is rescaled by a factor of $C_\pm\Delta\varphi$, all curves for positive potentials converge to a single curve that continues to capture the sign change for the current. By applying a suitable dimensionless scaling, a universal behavior could thus also be derived for the current. For all three cases we find that at low pressure values, the current is almost constant and that the potential-driven current I^{E} (dashed line) is dominant. As the pressure increases, the current transits into the pressure-driven I^{P} (dotted line) regime. Our results show that, in theory, it would be possible to push positively charged ions against their electrostatic gradient. Equation (60) shows that the ion current through the pore can also be differentiated into two regimes. We see that the current can not only be amplified by a hydrodynamic pressure difference, but can also overcome the electrostatic forces.

In [7], further regimes and transitions have been discovered, due to the effects of hydrodynamic boundary slip. In this work we did not take into account transitions triggered by hydrodynamic interfacial slip. Since these are important for a systematic understanding, they will be the subject of our future studies.

5.2 Impact of geometry and fluid flow on the ion flux

In this case study we consider the impact of geometry of the ion channel, where we restrict ourselves to axially symmetric cases. This has been investigated for many decades and the typical test cases are cylindrical, conical and trumpet shapes. Within this subsection we thus consider a trumpet shaped pore as illustrated in Figure 6 with length $L = 10$, $\delta = 0.01$ and radius

$$R(z) = 4\frac{R_1 - R_2}{L^2}(z^2 - zL) + R_1. \tag{61}$$

We chose $R_1 = 10$ and $R_2 = 1.5$. For the ion concentration we apply the following Dirichlet boundary conditions $c_{\pm}^{\text{out}} = c_{\pm}^{\text{in}} = 0.1$. We consider a surface charge on the channel wall of the form

$$\sigma(z) = \frac{q}{2}(\tanh((z - L_1)/\varepsilon) - \tanh((z - L_2)/\varepsilon)), \tag{62}$$

with $q = 1$, $L_1 = 0.1L$, $L_2 = L - L_1$ and $\varepsilon = 8$. In addition, we apply a potential difference with $\varphi^{\text{in}} = 8$, s.t. $\Delta\varphi = \varphi^{\text{in}} - \varphi^{\text{out}} = 8$. All other parameter values are given in Table 1 and Table 2.

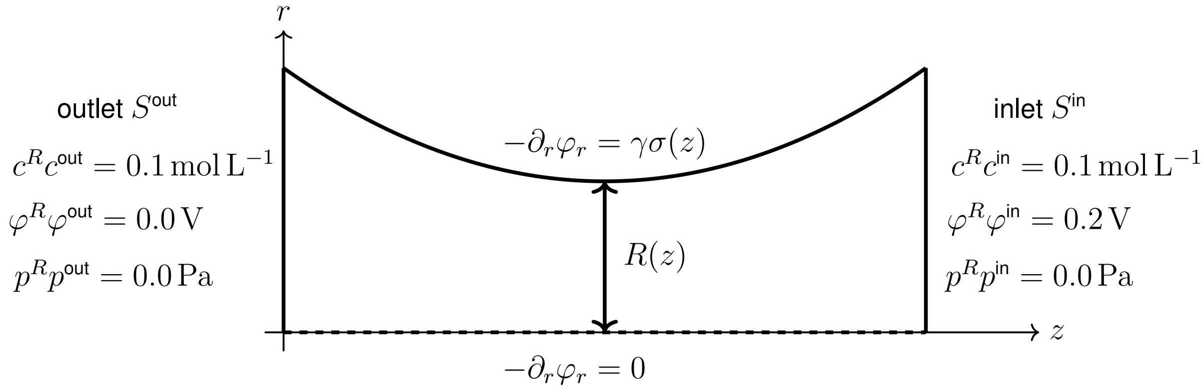

Figure 6: Illustration of a 2D axially symmetric trumpet shaped pore Ω. We apply a surface charge at $r = R(z)$ and a symmetry condition at $r = 0$ for the potential. At the inlet at $z = L$ and the outlet at $z = 0$ we apply Dirichlet boundary conditions for the concentrations, the potential and the pressure.

We calculated the solution for two different scenarios. In the first case, we have solved the classical PNP system given by the following equations (9a)-(9d) with $P_e = 0$. Note that such a system was also studied by Matejczyk et al. [22] for trumpet shaped pores. In the second case, we have solved the full problem including the coupling with Stokes equations. In both cases we calculated the steady state solution and find that, due to the positive surface charge on the channel wall, the anion concentration becomes high close to the pore wall and decreases towards the center of the pore (figures 7b, 7d and 7f). The cation concentration on the other hand has a maximum on the pore center and decreases towards the wall (figures 7a, 7c and 7e). Comparing the solutions for the concentrations from the classical PNP (dotted lines) with the PNPS system (solid lines and stars) we find that the fluid flow has an impact, especially on the cation concentration (Figure 7). For the cation concentration, we observe the greatest changes in the center of the pore at $r = 0$. At $z = 0.2\,L$ (Figure 7a) we find that the cation concentration decreases by 0.018. The decrease becomes more significant at the narrowest point where the concentration drops by 0.046 (Figure 7c). Close to the inlet on the other hand the additional advection term (due to the Stokes coupling) leads to an increase by 0.023 (Figure 7e). For the anions, however, the influence of hydrodynamic coupling is minimal. The average deviation between the PNP and PNPS solutions is only 0.18, which is negligible compared with the maximum concentration (≈ 10). Consequently, no substantial change in the anion distribution is observed across the pore cross-sections. Comparing the asymptotic model (solid lines) with the 2D FEM solution (stars) shows that the asymptotic approximation also captures the overall dynamics of the ion concentrations in a trumpet shaped pore with surface charge and applied potential difference.

The pressure is high at the pore walls and decreases towards the center of the pore (figures 8b, 8d and 8f). In the center of the pore at $r = 0$ (Figure 9b) the pressure is approximately zero close to outlet (Figure 8b) and the inlet (Figure 8f) while it reaches a maximum at around $z = 0.5\,L$, the narrowest point. Furthermore, we find that the velocity profile deviates along the pore: near the outlet (Figure 8a) and inlet (Figure 8e), the axial velocity decreases in the center of the pore (Figure 8c), even reversing its sign. At the narrowest point for $z = 0.5$, however, it approaches a parabolic profile, becoming larger in the center of the pore and decreasing toward the wall. Figure 9a shows that the velocity reaches a maximum at $z = 0.5\,L$ and changes sign at approximately $z = 0.1\,L$ and $z = 0.8\,L$, which corresponds exactly to the transitions from zero surface charge to a positive surface charge.

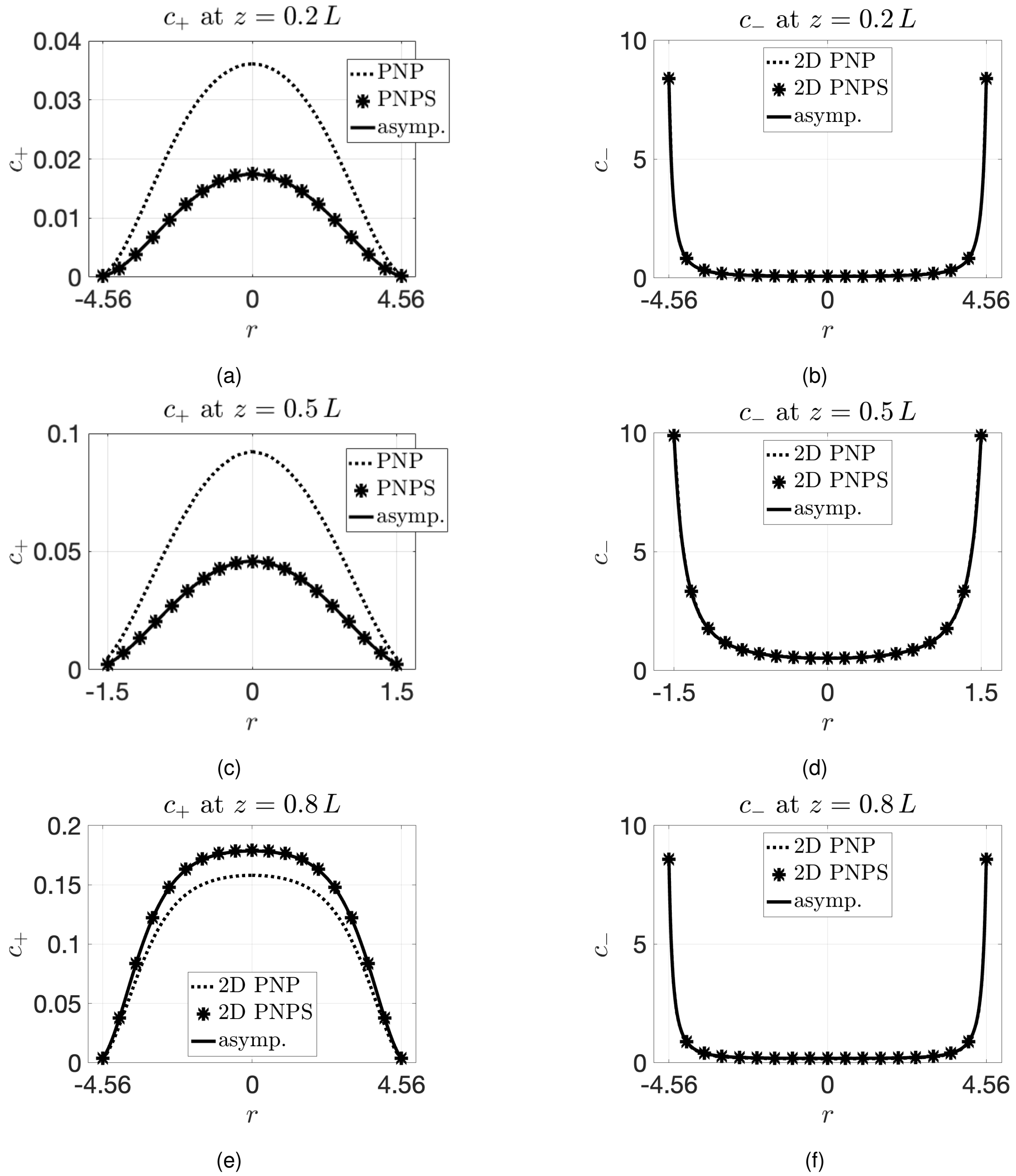

Figure 7: Ion concentrations for a trumpet shaped pore for two different scenarios: PNP equations (dotted line) and PNPS equations where we compare the 2D FEM solution from FEniCS (stars) to the asymptotic solution (solid line). The left column depicts the cation concentration, the right column the anion concentration.

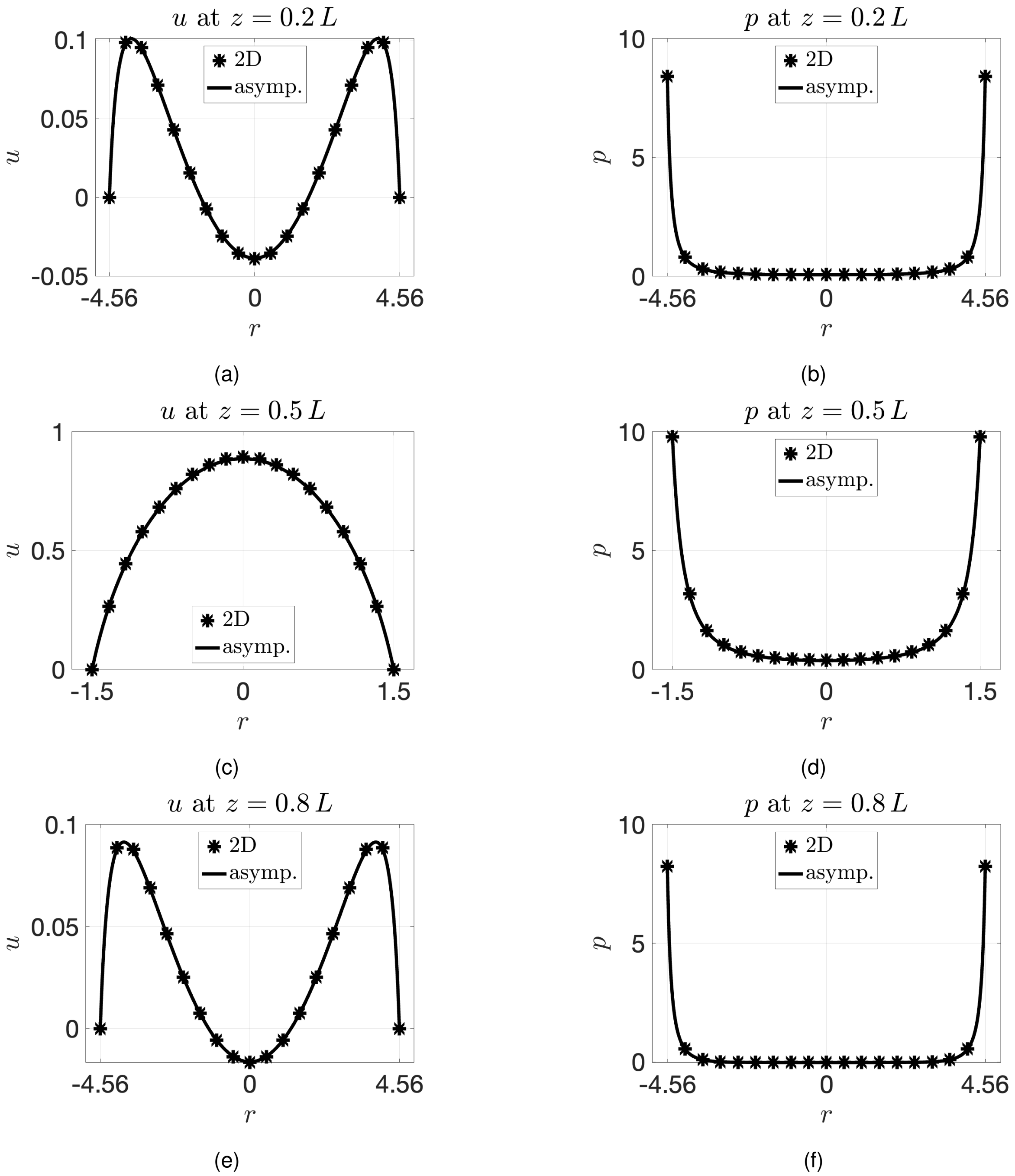

Figure 8: Comparison of 2D FEM FEniCS solutions (stars) for velocity and pressure with the asymptotic solution (solid line) for a trumpet shaped pore. The left column depicts the velocity, the right column the pressure.

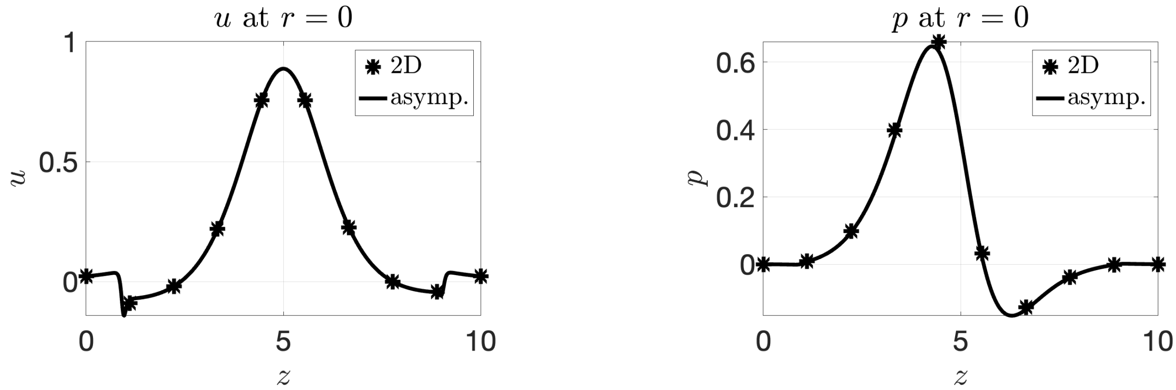

(a)

(b)

Figure 9: Comparison of 2D FEM FEniCS solution (stars) for velocity and pressure with the asymptotic solution (solid line) for a trumpet shaped pore in axial direction. (a) Velocity and (b) pressure at $r = 0$ plotted along the z-direction.

A closer look at the asymptotic model (equation (51a) for velocity) reveals that we have additional contributions in the axial pressure gradient (51b) resulting from the concentrations and the electrostatic potential. In addition, there is also a contribution from a radial pressure gradient, which is hidden in equation (50j) and also results from concentrations and the electrostatic potential. Furthermore, we could demonstrate that the bottle neck at $z = 0.5\,L$ of the trumpet shape leads to higher velocities and concentrations in this area, illustrating the impact of the geometry on the flux through the channel. In summary our asymptotic model accurately captures the impact of the fluid flow and the trumpet shape on the ion flux through the pore.

5.3 Conductivity in protein-based channels

Cytolysin A (ClyA) is a pore forming toxin that is released by some strains of *Escherichia coli* bacteria to damage host cells by creating pores in their membrane. Since ClyA forms stable nanopores, it is also often used in experimental ion channel studies and is therefore an important application example for the study of mathematical models [39]. The hydrophilic pore is around $15\,\mathrm{nm}$ long with a radius of around $1.65\,\mathrm{nm}$ at its narrowest point. More and more computational studies use geometry and charge density obtained by MD simulations to calculate IV-relations using a continuum description of the ion flux through the pore [21, 39, 40]. The geometry is often reconstructed using the contour lines of the charge density map of the proteins. However, solving the continuum model for the entire 3D domain is computationally intensive, and meshing the geometry is not trivial. To save computing costs, the MD geometry is therefore often reduced to an axially symmetric 2D domain. Since we have derived the asymptotic model for arbitrarily shaped pores with radius $R(z)$, we can use it to solve the model for more complex geometries derived from MD simulations without the need to define a mesh for it. To demonstrate this, we used the data of [39] in the supplementary information and reconstructed the axially symmetric 2D shape of the ClyA pore. Our simulation domain is given in Figure 10. The pore is placed between two reservoirs of length 2 each with $\delta = 0.1$, i.e. the entry of the pore is at $z = 2$ and the outlet at $z = 3.5$. The length of the overall domain is $L = 5.5$. The two bath have a maximum radius of $R(z = 0) = R(z = 5.5) = 5$ and narrow linearly toward the pore. We consider a mixture of $K_+ = c_+$ and $Cl_- = c_-$, with $c_\pm^{\text{out}} = c_\pm^{\text{in}} = c^{\text{bulk}}$ at $z = 0$ and $z = 5.5$. In addition, we apply a potential difference of $\Delta\varphi = \varphi^{\text{in}} - \varphi^{\text{out}}$ with φ^{out} at $z = 0$ and φ^{in} at $z = 5.5$. If not explicitly mentioned otherwise in the text the parameter values were chosen as given in Table 1 and Table 4. We apply a constant surface charge of $q = -0.25$ given by equation (62) with $L_1 = 2$, $L_2 = 3.5$ and $\varepsilon = 0.5$.

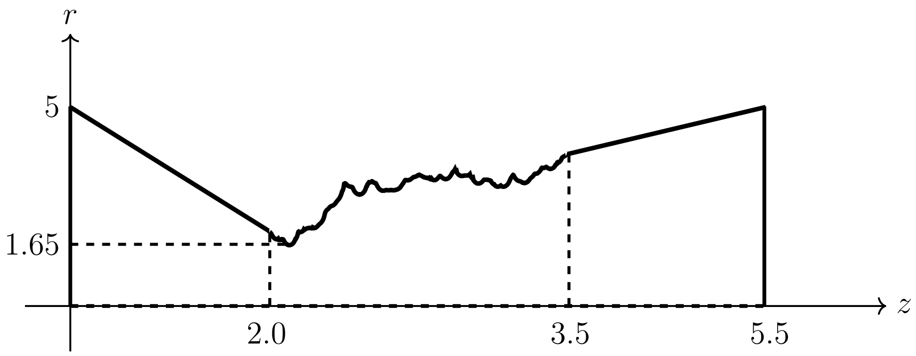

Figure 10: Illustration of a 2D axially symmetric trumpet shaped pore Ω. We apply a homogeneous surface charge at S^{wall}, i.e. $r = R(z)$ for the potential. At the inlet S^{in} at $\tilde{z} = 55\,\text{nm}$ and the outlet S^{out} at $\tilde{z} = 0\,\text{nm}$ we apply Dirichlet boundary conditions for the concentrations, the potential and the pressure. The shape of the pore $2 \leq z \leq 3.5$ was taken from the supplementary data from [39]

We calculated the transport coefficients for varying concentrations through the pore given by $t_\pm = I_\pm/(I_+ + I_-)$. For our simplified model we find that it is capable to capture the overall behavior of ion flux through the pore. Figure 11a shows the cation transport coefficient t_+ as a function of concentration for two different potentials $\Delta\varphi = \pm 6$ (solid line and crosses, respectively).

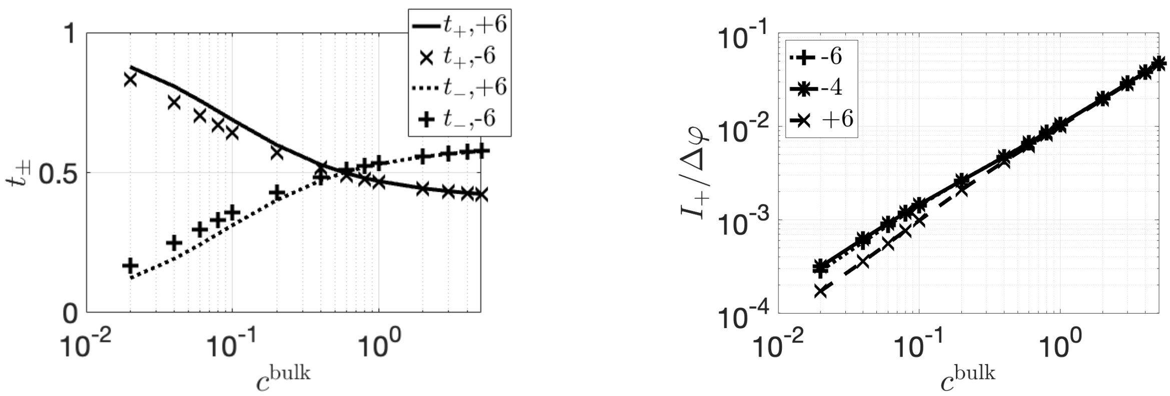

(a) (b)

Figure 11: (a) Transport coefficients for the cations (solid line and crosses) and anions for (dotted line and plus signs) for $\Delta\varphi = \pm 6$ for varying salt concentrations. (b) Cation conductance for $\Delta\varphi = -6$ (plus signs), $\Delta\varphi = -4$ (stars) and $\Delta\varphi = 6$ (crosses).

While for small concentrations the ion conductance of the pore is mainly driven by the cation current, t_+ decreases with increasing concentration. Therefore, we find that the anion transport t_- increases with increasing concentration (dotted line and plus signs) until the overall conductance is driven by the anion current. A switch in the selectivity of the pore can be observed at around $c^{\text{bulk}} = 0.5$. Note that for the ePNP-NS model including steric effects in Willems et al. [39] this switch was reported at $c^{\text{bulk}} = 2$. In addition to steric effects, our current model also does not yet take into account the charge density of the protein. We assume a homogeneous negative surface charge throughout the pore, as Willems et al. reported a preferred cation selectivity in their work. However, we plan to take the coupling with charge density into account in future work. As in section 5.1 we also calculated the cation conductance which is the current scaled with the applied potential difference $I_\pm/\Delta\varphi$ and plotted it for varying salt concentrations (Figure 11b). Again we observe that for all applied potentials the curves fall into one master curve for high enough concentrations. For small concentrations we still observe a rightward (or leftward) shift of the curves.

We also evaluated the velocity at $z = 2.08$ for $\Delta\varphi = -4$ and four different concentrations (Figure 12a). Similar as reported by Willems et al. [39] we find that the velocity in the center of the pore at $r = 0$ at first increases by increasing the concentrations form $c^{\text{bulk}} = 0.005$ (solid) up to $c^{\text{bulk}} = 0.15$. However, if we further increase the concentration to $c^{\text{bulk}} = 0.75$ and $c^{\text{bulk}} = 5$ we find that the velocity has decreased each time.

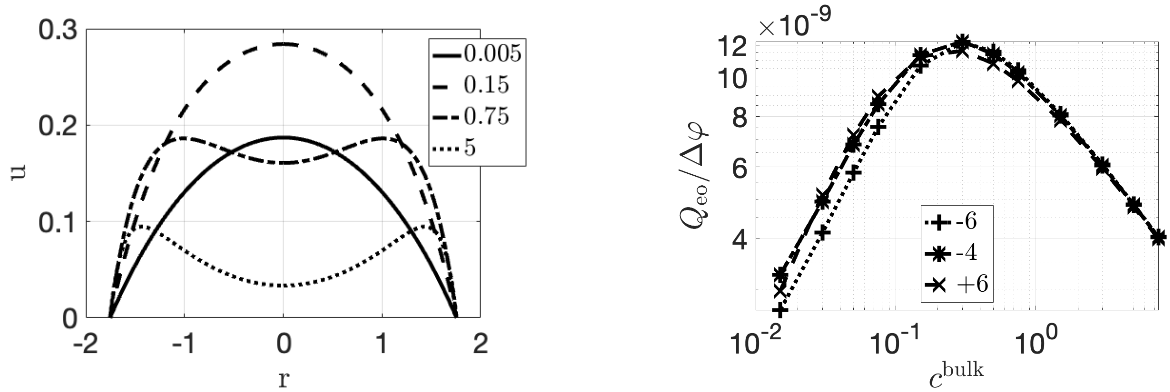

(a)

(b)

Figure 12: (a) Velocity calculated for different concentrations c^{bulk}. (b) Flow rate plotted as a function of c^{bulk} for $\Delta\varphi = 6$ (crosses), $\Delta\varphi = -4$ (stars) and $\Delta\varphi = -6$ (plus signs).

Plotting the flow rate $Q_{eo} = \int_S \mathbf{v} \cdot \mathbf{n}\, \mathrm{d}S = \int_0^{R(z)} u^0 r\, \mathrm{d}r$ at $z = 2.08$ as a function of concentration (Figure 12b) better illustrates this phenomenon. As noted in section 5.1, scaling the flow with $\Delta\varphi$ causes the different maxima for different potentials of the same sign. Up to a concentration of $c^{\text{bulk}} = 0.3$, the flow increases, reaches its maximum of $Q_{eo}/\Delta\varphi = 12e - 9$ for $\Delta\varphi = -4$ (stars) and $\Delta\varphi = \pm 6$ (crosses and plus signs) there, and then decreases again for increasing concentrations. Values reported by Willems et al. [39] are again different, they report a maximum of $\tilde{Q}_{eo}/\Delta\tilde{\varphi} = 11.5\,\mathrm{nm}^3\,\mathrm{ns}^{-1}\,\mathrm{V}^{-1}$ at $\tilde{c}^{\text{bulk}} = 0.5\,\mathrm{mol}\,\mathrm{L}^{-1}$ while we find a maximum of $\tilde{Q}_{eo}/\Delta\tilde{\varphi} = 4.7\,\mathrm{nm}^3\,\mathrm{ns}^{-1}\,\mathrm{V}^{-1}$ at $c^{\text{bulk}} = 0.3\,\mathrm{mol}\,\mathrm{L}^{-1}$.

In summary it is possible to use pore-shapes obtained from MD simulations to capture the general dynamics in such channels with our asymptotic model. The observed deviations are due to the 2D model used. Since we only need to know the coordinates for the boundary in order to solve the equations for the asymptotic model, it is not necessary to define a mesh on such an irregular domain, thus saving an often very time-consuming step.

Furthermore, we could show that scaling laws derived from simpler models, such as those for straight pores, can also be applied to more complex problems.

6 Conclusion and Outlook

The asymptotic model developed in this work provides a mathematically systematic and physically transparent framework for describing ion transport in narrow channels. Our approach complements and clarifies earlier one-dimensional reductions, such as those introduced by Fair and Osterle [11] and later extended by Rankin et al. [27]. These classical models are based on lubrication theory, but lack a rigorous derivation from the complete PNPS system and typically require a numerical evaluation of the first-order axial pressure gradient. In contrast, the present analysis identifies a distinct asymptotic region in which the Debye length is comparable to the channel width, leading to a closed-form analytical description for pressure and velocity that recovers previous reductions as limiting cases while significantly extending their range of validity. We have shown that the volumetric flow in a cylindrical pore with homogeneous surface charge smoothly transitions between an potential-dominated and a pressure-driven regime. For small Debye layers the volumetric flow can be expressed as a combination of two classical limits: in the potential-dominated case, it reduces to the Helmholtz-Smoluchowski approximation, while in the limit of strong hydrodynamic pressure gradient, it approaches the Poiseuille profile. A similar transition occurs in ion currents. Depending on the applied voltage and the pressure gradient, the total current shifts between an potential-controlled and a pressure-controlled regime, reflecting the coupled electrohydrodynamic response of the system. Furthermore, our calculations show that a correction is necessary for large Debye layers. The EDL axial force density therefore provides an additional flow contribution and is necessary, for example, for low salt concentrations when the surface charge cannot be sufficiently screened.

The flexibility of the asymptotic framework opens up several possibilities for further development. A natural extension concerns the inclusion of hydrodynamic slip at the channel walls. The slip can be included in the reduced Stokes problem as a first approximation, where its effects on the flow field can be profound. Even without electrostatic forces, different slip length scales can fundamentally alter flow resistance, induce transitions between plug-like and shear-dominated profiles, and modify pressure-flow relationships [24,26]. Previous studies [9,25] have highlighted the complexity of such slip-induced transitions, and a systematic investigation of their interaction with electroviscous and electroosmotic effects represents an important direction for future work.

In addition to electrostatic and hydrodynamic forces, there are other properties of nanopores that influence ion transport through the pore. In particular, geometric constraints and deviations from ideal cylindrical symmetry can have a strong influence on ion flow and IV properties. Fluctuations in pore radius can lead to spatially heterogeneous electric fields and uneven local conductivities. These geometric features can influence ion selectivity and surface charge regulation and promote rectification, thereby affecting overall transport behavior. Such effects are particularly evident when the characteristic pore dimensions approach the Debye length or when multivalent ions or finite size effects are present.

Incorporating these geometric complexities into the asymptotic framework allows for a more comprehensive understanding of how shape, surface chemistry, and flow collectively control ion transport in realistic nanofluidic systems. Our asymptotic framework accounts for such axial variations in pore radius and, as illustrated by trumpet-shaped and protein-based pores obtained from MD simulations, accurately captures their associated geometric effects. In our investigation of a trumpet-shaped pore, we observe that ion concentrations vary systematically from the wider areas toward the bottleneck, and this axial variation is further amplified by the coupling between ion transport and local fluid velocity. The asymptotic model shows that the varying geometry induces an additional pressure gradient that depends on the ion concentrations. This becomes particularly clear when examining the fluid velocity and ion conductivity as a function of ion concentration in a ClyA-based channel obtained from MD simulations. Both variables increase with rising salt concentration, but begin to decrease once a certain threshold value is reached. Taken together, these observations illustrate how geometry and flow jointly influence the nonlinear transport response of the system.

Although the PNPS model provides a successful continuum-level description of electrokinetic transport, it neglects ion–ion correlations, finite-volume constraints, hydration effects, and non-ideal thermodynamics. These limitations become particularly pronounced in nanoscale confinement or under strong electric fields, where classical assumptions, such as point-like ions and linearized electrostatics, break down. Extensions of this system include ion-ion interactions and size-exclusion effects, as well as hydration effects of the ions, which play an important role in the selective passage of ion channels [12, 17, 20, 28]. Including such refined thermodynamic descriptions into the current asymptotic reduction would enable a unified multiscale framework capable of capturing both continuum transport and molecular-level influences such as charges distributions.

Taken together, these future extensions illustrate the versatility and potential of the derived reduced model. By providing analytical insights and computational efficiency across a wide range of parameters, the framework presented here provides a solid foundation for investigating electrohydrodynamic phenomena in biological ion channels, synthetic nanopores, and new nanofluidic technologies.

Acknowledgements

The authors would like to thank Dirk Peschka for his support with FEniCS and Python.

References

[1] N. Bavi, D. M. Cortes, C. D. Cox, P. R. Rohde, W. Liu, J. W. Deitmer, O. Bavi, P. Strop, A. P. Hill, D. Rees, et al. The role of mscl amphipathic n terminus indicates a blueprint for bilayer-mediated gating of mechanosensitive channels. *Nature communications*, 7(1):11984, 2016.

[2] L. Bocquet and E. Charlaix. Nanofluidics, from bulk to interfaces. *Chemical Society Reviews*, 39(3):1073–1095, 2010.

[3] D. Branton, D. W. Deamer, A. Marziali, H. Bayley, S. A. Benner, T. Butler, M. Di Ventra, S. Garaj, A. Hibbs, X. Huang, et al. The potential and challenges of nanopore sequencing. *Nature biotechnology*, 26(10):1146–1153, 2008.

[4] D. Cohen-Tanugi and J. C. Grossman. Water desalination across nanoporous graphene. *Nano Letters*, 12(7):3602–3608, June 2012.

[5] C. D. Cox, N. Bavi, and B. Martinac. Biophysical principles of ion-channel-mediated mechanosensory transduction. *Cell reports*, 29(1):1–12, 2019.

[6] R. V. Craster and O. K. Matar. Dynamics and stability of thin liquid films. *Reviews of modern physics*, 81(3):1131–1198, 2009.

[7] T. Curk, S. G. Leyva, and I. Pagonabarraga. Discontinuous transition in electrolyte flow through charge-patterned nanochannels. *Physical Review Letters*, 133(7):078201, Aug. 2024.

[8] S. Dal Cengio and I. Pagonabarraga. Confinement-controlled rectification in a geometric nanofluidic diode. *The Journal of Chemical Physics*, 151(4), 2019.

[9] S. Datta and J. Choudhary. Effect of hydrodynamic slippage on electro-osmotic flow in zeta potential patterned nanochannels. *Fluid Dynamics Research*, 45(5):055502, 2013.

[10] W. Dreyer, C. Guhlke, and R. Müller. Overcoming the shortcomings of the nernst–planck model. *Physical Chemistry Chemical Physics*, 15(19):7075, 2013.

[11] J. Fair and J. Osterle. Reverse electrodialysis in charged capillary membranes. *The Journal of Chemical Physics*, 54(8):3307–3316, 1971.

[12] D. Gillespie. Energetics of divalent selectivity in a calcium channel: the ryanodine receptor case study. *Biophysical journal*, 94:1169–1184, Feb. 2008.

[13] Y. Green. Ion transport in nanopores with highly overlapping electric double layers. *The Journal of Chemical Physics*, 154(8), Feb. 2021.

[14] Y. Green. Effects of surface-charge regulation, convection, and slip lengths on the electrical conductance of charged nanopores. *Physical Review Fluids*, 7(1):013702, Jan. 2022.

[15] C. C. Harrell, P. Kohli, Z. Siwy, and C. R. Martin. Dna- nanotube artificial ion channels. *Journal of the American Chemical Society*, 126(48):15646–15647, 2004.

[16] L. Jubin, A. Poggioli, A. Siria, and L. Bocquet. Dramatic pressure-sensitive ion conduction in conical nanopores. *Proceedings of the National Academy of Sciences*, 115(16):4063–4068, 2018.

[17] C. Keller, M. Landstorfer, J. Fuhrmann, and B. Wagner. A model framework for ion channels with selectivity filters based on non-equilibrium thermodynamics. *Entropy*, 27(9):981, Sept. 2025.

[18] M. H. Köhler, J. R. Bordin, and M. C. Barbosa. 2d nanoporous membrane for cation removal from water: Effects of ionic valence, membrane hydrophobicity, and pore size. *The Journal of Chemical Physics*, 148(22), Feb. 2018.

[19] M. Li and M. Muthukumar. Electro-osmotic flow in nanoconfinement: Solid-state and protein nanopores. *The Journal of Chemical Physics*, 160(8), Feb. 2024.

[20] J.-L. Liu and B. Eisenberg. Correlated ions in a calcium channel model: A poisson–fermi theory. *The Journal of Physical Chemistry B*, 117(40):12051–12058, sep 2013.

[21] J.-L. Liu and B. Eisenberg. Molecular mean-field theory of ionic solutions: A poisson-nernst-planck-bikerman model. *Entropy*, 22(5):550, may 2020.

[22] B. Matejczyk, J.-F. Pietschmann, M.-T. Wolfram, and G. Richardson. Asymptotic models for transport in large aspect ratio nanopores. *European Journal of Applied Mathematics*, 30(3):557–584, June 2018.

[23] A. Meller. A new tool for cell signalling research. *Nature Nanotechnology*, 14(8):732–733, 2019.

[24] A. Münch, B. Wagner, and T. P. Witelski. Lubrication models with small to large slip lengths. *Journal of Engineering Mathematics*, 53(3):359–383, 2005.

[25] H. Park and T. Kim. Extension of the helmholtz-smoluchowski velocity to the hydrophobic microchannels with velocity slip. *Lab on a Chip*, 9(2):291–296, 2009.

[26] D. Peschka, S. Haefner, L. Marquant, K. Jacobs, A. Münch, and B. Wagner. Signatures of slip in dewetting polymer films. *Proceedings of the National Academy of Sciences*, 116(19):9275–9284, 2019.

[27] D. J. Rankin and D. M. Huang. The effect of hydrodynamic slip on membrane-based salinity-gradient-driven energy harvesting. *Langmuir*, 32(14):3420–3432, 2016.

[28] R. Roth and D. Gillespie. Shells of charge: a density functional theory for charged hard spheres. *Journal of Physics: Condensed Matter*, 28(24):244006, Apr. 2016.

[29] O. Rybalkina, K. Tsygurina, V. Sarapulova, S. Mareev, V. Nikonenko, and N. Pismenskaya. Evolution of current–voltage characteristics and surface morphology of homogeneous anion-exchange membranes during the electrodialysis desalination of alkali metal salt solutions. *Membranes and Membrane Technologies*, 1(2):107–119, 2019.

[30] J. Saharia, Y. M. N. D. Y. Bandara, B. I. Karawdeniya, C. Hammond, G. Alexandrakis, and M. J. Kim. Modulation of electrophoresis, electroosmosis and diffusion for electrical transport of proteins through a solid-state nanopore. *RSC Advances*, 11(39):24398–24409, 2021.

[31] R. B. Schoch, J. Han, and P. Renaud. Transport phenomena in nanofluidics. *Reviews of modern physics*, 80(3):839–883, 2008.

[32] A. Singer, D. Gillespie, J. Norbury, and R. S. Eisenberg. Singular perturbation analysis of the steady-state poisson–nernst–planck system: Applications to ion channels. *European Journal of Applied Mathematics*, 19(5):541–560, oct 2008.

[33] Z. Siwy, E. Heins, C. C. Harrell, P. Kohli, and C. R. Martin. Conical-nanotube ion-current rectifiers: the role of surface charge. *Journal of the American Chemical Society*, 126(35):10850–10851, 2004.

[34] A. D. Stroock, M. Weck, D. T. Chiu, W. T. Huck, P. J. Kenis, R. F. Ismagilov, and G. M. Whitesides. Patterning electro-osmotic flow with patterned surface charge. *Physical review letters*, 84(15):3314, 2000.

[35] S. P. Surwade, S. N. Smirnov, I. V. Vlassiouk, R. R. Unocic, G. M. Veith, S. Dai, and S. M. Mahurin. Water desalination using nanoporous single-layer graphene. *Nature Nanotechnology*, 10(5):459–464, Mar. 2015.

[36] C. Wang, S. Sensale, Z. Pan, S. Senapati, and H.-C. Chang. Slowing down dna translocation through solid-state nanopores by edge-field leakage. *Nature Communications*, 12(1), Jan. 2021.

[37] M. Wanunu, J. Sutin, and A. Meller. Dna profiling using solid-state nanopores: detection of dna-binding molecules. *Nano letters*, 9(10):3498–3502, 2009.

[38] G. B. Whitham. *Linear and nonlinear waves*. John Wiley & Sons, 2011.

[39] K. Willems, D. Ruić, F. L. R. Lucas, U. Barman, N. Verellen, J. Hofkens, G. Maglia, and P. Van Dorpe. Accurate modeling of a biological nanopore with an extended continuum framework. *Nanoscale*, 12(32):16775–16795, 2020.

[40] D. Xie. An efficient finite element iterative method for solving a nonuniform size modified poisson-boltzmann ion channel model. *Journal of Computational Physics*, 470:111556, Dec. 2022.

Appendix

A Auxiliary calculations for the large aspect ratio asymptotics

Poisson equation. In order to solve equation (17)

$$0 = \int_0^{R(z)} \partial_r (r \partial_r \varphi^1)\,\mathrm{d}r + \int_0^{R(z)} \partial_z (\partial_z \varphi^0) r\,\mathrm{d}r, \tag{63}$$

we went through the following steps. Switching integration and differentiation in the second integral gives

$$\int_0^{R(z)} \partial_z (\partial_z \varphi^0) r\,\mathrm{d}r = -R'(z) \partial_z \varphi^0|_{r=R(z)} + \partial_z \int_0^{R(z)} \partial_z \varphi^0 r\,\mathrm{d}r. \tag{64}$$

Since the $\mathcal{O}(\delta^2)$-order term of the surface charge boundary condition (10c) yields

$$\partial_r \varphi^1|_{r=R(z)} - R'(z) \partial_z \varphi^0|_{r=R(z)} = 0, \tag{65}$$

we obtain

$$\begin{aligned} 0 &= \int_0^{R(z)} \partial_r (r \partial_r \varphi^1)\,\mathrm{d}r + \int_0^{R(z)} \partial_z (\partial_z \varphi^0) r\,\mathrm{d}r \\ &= R(z) \underbrace{\left(\partial_r \varphi^1|_{r=R(z)} - R'(z) \partial_z \varphi^0|_{r=R(z)}\right)}_{=0} + \partial_z \int_0^{R(z)} \partial_z \varphi^0 r\,\mathrm{d}r \\ &= \partial_z \int_0^{R(z)} \partial_z \varphi_z^0 r\,\mathrm{d}r. \end{aligned}$$

Nernst-Planck equation. In order to solve equation (27) we introduced the stream function

$$s = \int_0^r u^0 r\,\mathrm{d}r, \tag{66}$$

with $u^0 = r^{-1} \partial_r s$ and $w = -r^{-1} \partial_z s$, such that

$$\begin{aligned} \partial_t c_\pm &= -P_e \int_0^{R(z)} \left(w \partial_r c_\pm^0 + u^0 \partial_z c_\pm^0\right)\,\mathrm{d}r + \int_0^{R(z)} \partial_z f_\pm^0 r\,\mathrm{d}r + \int_0^{R(z)} \partial_r \left(r g_\pm^1\right)\,\mathrm{d}r \\ &= -P_e \int_0^{R(z)} \left(-\partial_z s \partial_r c_\pm^0 + \partial_r s \partial_z c_\pm^0\right)\,\mathrm{d}r + \int_0^{R(z)} \partial_z f_\pm^0 r\,\mathrm{d}r + \int_0^{R(z)} \partial_r \left(r g_\pm^1\right)\,\mathrm{d}r. \end{aligned} \tag{67}$$

We rewrite the first integral such that

$$\begin{aligned} &\int_0^{R(z)} \left(-\partial_z s \partial_r c_\pm^0 + \partial_r s \partial_z c_\pm^0\right)\,\mathrm{d}r \\ &\quad= \int_0^{R(z)} \left[-\partial_z (c_\pm^0 \partial_r s) + c_\pm^0 \partial_z (\partial_r s) + \partial_r (c_\pm^0 \partial_z s) - c_\pm^0 \partial_z (\partial_r s)\right]\,\mathrm{d}r \\ &\quad= -\int_0^{R(z)} \partial_z (c_\pm^0 \partial_r s)\,\mathrm{d}r + \int_0^{R(z)} \partial_r (c_\pm^0 \partial_z s)\,\mathrm{d}r. \end{aligned} \tag{68}$$

Changing integration and differentiation in the first integral and solving the second integral further yields

$$
\begin{aligned}
&-\int_0^{R(z)} \partial_z(c_\pm^0 \partial_r s)\,\mathrm{d}r + \int_0^{R(z)} \partial_r(c_\pm^0 \partial_z s)\,\mathrm{d}r \\
&\quad= -\partial_z \int_0^{R(z)} c_\pm^0 \partial_r s\,\mathrm{d}r + c_\pm^0 \partial_r s|_{r=R(z)} R'(z) + c_\pm^0 \partial_z s|_{r=R(z)} - c_\pm^0 \partial_z s|_{r=0} \\
&\quad= -\partial_z \int_0^{R(z)} c_\pm^0 \partial_r s\,\mathrm{d}r.
\end{aligned} \tag{69}
$$

Due to the no-slip condition $u^0|_{r=R(z)} = w^0|_{r=R(z)} = 0$ also $\partial_r s|_{r=R(z)} = 0$ and $\partial_z s|_{r=R(z)} = 0$ and with the symmetry condition $\partial_z s|_{r=0} = 0$. Using this result we have

$$
\begin{aligned}
\partial_t c_\pm &= -P_e \int_0^{R(z)} \left(-\partial_z s \partial_r c_\pm^0 + \partial_r s \partial_z c_\pm^0\right)\,\mathrm{d}r + \int_0^{R(z)} \partial_z f_\pm^0 r\,\mathrm{d}r + \int_0^{R(z)} \partial_r\left(r g_\pm^1\right)\,\mathrm{d}r \\
&= P_e \partial_z \int_0^{R(z)} c_\pm^0 \partial_r s\,\mathrm{d}r + \partial_z \int_0^{R(z)} f_\pm^0 r\,\mathrm{d}r - R(z)\underbrace{\left(R'(z) f_\pm^0|_{r=R(z)} - g_\pm^1|_{r=R(z)}\right)}_{=} 0 \\
&= P_e \partial_z \int_0^{R(z)} c_\pm^0 u^0 r\,\mathrm{d}r + k_\pm \partial_z \int_0^{R(z)} \left(\partial_z c_\pm^0 \pm c_\pm^0 \partial_z \varphi^0\right) r\,\mathrm{d}r,
\end{aligned} \tag{70}
$$

with the boundary condition (71)

$$
R'(z) f_\pm^0|_{r=R(z)} - g_\pm^1|_{r=R(z)} = 0. \tag{71}
$$

B Velocity in a cylindrical pore

Since we want to reconstruct the Hagen-Poiseuille and Helmholtz-Smoluchowski approximation we will calculate the volumetric flow $\langle u^0 \rangle = \int_0^L \int_0^R u^0 r\,\mathrm{d}r\,\mathrm{d}z$. At first we will integrate $u^0(r,z)$ given by equation 51a in z-direction from 0 to L. Starting with the first term $\partial_z p_z^0$ yields

$$
\frac{1}{4}(r^2 - R^2) \int_0^L \partial_z p_z^0\,\mathrm{d}z = -\frac{1}{4}(r^2 - R^2)\Delta p. \tag{72}
$$

For the K_2–terms we have

$$
\begin{aligned}
\langle u^{\mathsf{EDL}} \rangle_r &= \int_{z=0}^L (K_2(r,z) - K_2(r=R,z))\,\mathrm{d}z \\
&= \int_0^r \frac{1}{r} \int_0^r \int_{z=0}^L ((\partial_z p_r^0) r - \Lambda^2 (\partial_z \varphi_r^0) \partial_r (r \partial_r \varphi_r^0))\,\mathrm{d}z (\,\mathrm{d}r)^2 \\
&\quad - \int_0^r \frac{1}{r} \int_0^r \int_{z=0}^L ((\partial_z p_r^0) r - \Lambda^2 (\partial_z \varphi_r^0) \partial_r (r \partial_r \varphi_r^0))\,\mathrm{d}z (\,\mathrm{d}r)^2|_{r=R} \\
&= -\Lambda^2 \int_{z=0}^L \int_0^r \frac{1}{r} \int_0^r (\partial_z \varphi_r^0) \partial_r (r \partial_r \varphi_r^0) (\,\mathrm{d}r)^2\,\mathrm{d}z \\
&\quad + \Lambda^2 \int_{z=0}^L \int_0^r \frac{1}{r} \int_0^r (\partial_z \varphi_r^0) \partial_r (r \partial_r \varphi_r^0) (\,\mathrm{d}r)^2|_{r=R}\,\mathrm{d}z,
\end{aligned} \tag{73}
$$

since $\int_{z=0}^{L} \partial_z p_r^0 \, \mathrm{d}z = 0$ due to $p_r^0|_{z=0} = p_r^0|_{z=L} = 0$. For the last term in (39a) we simply have

$$\frac{\Delta\varphi}{L}\Lambda^2 \int_{z=0}^{L} \left[\varphi_r^0 - \varphi_r^0|_{r=R}\right] \, \mathrm{d}z, \tag{74}$$

such that the flow in z-direction is

$$\langle u^0\rangle_r(r) = -\Delta p \frac{1}{4}(r^2 - R^2) + \frac{\Delta\varphi}{L}\Lambda^2 \int_{z=0}^{L} \left[\varphi_r^0 - \varphi_r^0|_{r=R}\right] \, \mathrm{d}z + \langle u^{\mathsf{EDL}}\rangle_r. \tag{75}$$

Next, we integrate in r-direction from 0 to R

$$\langle u^0\rangle = \int_0^R \langle u^0\rangle_r \, r \, \mathrm{d}r = \Delta p \frac{1}{16} R^4 - \frac{\Delta\varphi}{L}\Lambda^2 \langle\zeta\rangle + \langle u^{\mathsf{EDL}}\rangle, \tag{76}$$

with

$$\langle\zeta\rangle = \int_{z=0}^{L}\int_{r=0}^{R} \left[\varphi_r^0 - \varphi_r^0|_{r=R}\right] r \, \mathrm{d}r \, \mathrm{d}z \tag{77}$$

and

$$\begin{aligned}\langle u^{\mathsf{EDL}}\rangle = &\int_{z=0}^{L}\int_{r=0}^{R} r \int_0^r \frac{1}{r}\int_0^r (\partial_z\varphi_r^0)(c_+^0 - c_-^0) r (\, \mathrm{d}r)^3 \, \mathrm{d}z \\ &- \frac{1}{2}R^2 \int_{z=0}^{L}\int_0^r \frac{1}{r}\int_0^r (\partial_z\varphi_r^0)(c_+^0 - c_-^0) r (\, \mathrm{d}r)^2|_{r=R} \, \mathrm{d}z,\end{aligned} \tag{78}$$

with equation (46a).

$$\langle u^0\rangle = \Delta p \frac{1}{16} R^4 - \frac{\Delta\varphi}{L}\Lambda^2 \langle\zeta\rangle + \langle u^{\mathsf{EDL}}\rangle. \tag{79}$$

C Current for a cylindrical pore

We find that in a cylindrical pore, i.e. a straight pipe, the current given by equation (52a) can further be simplified. We therefore calculate the current at the outlet $z = 0$, such that

$$I_\pm|_{z=0} = \pm 2\pi \int_0^R \left[k_\pm \mathrm{e}^{\mp\varphi_r^0} \left(\partial_z Q_\pm \pm Q_\pm \frac{\Delta\varphi}{L}\right) - P_e Q_\pm u^0 \mathrm{e}^{\mp\varphi_r^0}\right]_{z=0} r \, \mathrm{d}r. \tag{80}$$

At the outlet we assume that φ_r^0 is small, such that $\mathrm{e}^{\mp\varphi_r^0|_{z=0}} \approx 1 \mp \varphi_r^0|_{z=0} \approx 1$. We further have $Q_\pm \mathrm{e}^{\mp\varphi_r^0}|_{z=0} = c_\pm^{\mathsf{out}}$ and for the velocity we write

$$\int_0^R u^0|_{z=0} r \, \mathrm{d}r = \frac{\langle u^0\rangle}{L}. \tag{81}$$

All together we can approximate the current flowing through the outlet by

$$\begin{aligned} I_\pm|_{z=0} &= \pm 2\pi \int_0^R \left[k_\pm \mathrm{e}^{\mp\varphi_r^0} \left(\partial_z Q_\pm \pm Q_\pm \frac{\Delta\varphi}{L}\right) - P_e Q_\pm u^0 \mathrm{e}^{\mp\varphi_r^0}\right]_{z=0} r \, \mathrm{d}r \\ &= 2\pi \int_0^R k_\pm \left(\pm\partial_z Q_\pm|_{z=0} + c_\pm^{\mathsf{out}} \frac{\Delta\varphi}{L}\right) r \, \mathrm{d}r \mp 2\pi P_e c_\pm^{\mathsf{out}} \frac{\langle u^0\rangle}{L} \\ &= 2\pi \left[k_\pm \frac{1}{2}R^2 \left(\pm\partial_z Q_\pm|_{z=0} + c_\pm^{\mathsf{out}}\frac{\Delta\varphi}{L}\right) \mp P_e c_\pm^{\mathsf{out}} \left(\frac{\Delta p}{L}\frac{1}{16}R^4 - \Lambda^2 \frac{\Delta\varphi}{L}\frac{\langle\zeta\rangle}{L} + \frac{\langle u^{\mathsf{EDL}}\rangle}{L}\right)\right] \\ &= \pm 2\pi k_\pm \frac{1}{2} R^2 \partial_z Q_\pm|_{z=0} + 2\pi c_\pm^{\mathsf{out}} \left[\frac{\Delta\varphi}{L}\left(\frac{k_\pm}{2}R^2 + P_e \Lambda^2 \frac{\langle\zeta\rangle}{L}\right) \mp P_e \frac{\Delta p}{L}\frac{1}{16}R^4 \mp P_e \frac{\langle u^{\mathsf{EDL}}\rangle}{L}\right]. \end{aligned} \tag{82}$$

D Numerical scheme for the asymptotic model

In order to calculate the asymptotic model we need to solve equation (46a) for $\varphi_r^0(r,z)$ for every $z \in [0,L]$ with the respective boundary condition (46b). Once we have the solution for the potential we can solve equation (47a) for $Q_\pm(z)$ with the boundary condition (47c) to obtain $c_\pm^0(r,z)$. Note that in order to solve (47a) we also have to calculate the integrals (47b) which also depend on $u^0(r,z)$ and $\varphi_z^0(z)$. Once we have the solution for the concentrations and the potential we solve equation (51a) for the velocity $u^0(r,z)$ and equation (50a) for the pressure $p^0(r,z)$. This procedure is repeated until the maximum number of iteration max_iter is reached or the solutions have converged, such that $err < \epsilon$. We solve the three coupled ordinary differential equations (ODEs) in FEniCS using FEM.

Algorithm 1 Numerical scheme to calculate φ_r^0 and $Q_\pm$

Set $Q_\pm^0 = c_\pm^{\text{init}} \mathrm{e}^{\mp\varphi_r^{\text{init}}}$ for $z \in [0,L]$;
Set $\varphi^0 = \varphi^{\text{init}}$, $p^0 = p^{\text{init}}$ and $u^0 = u^{\text{init}}$ for $r \in [0,R(z)]$ and $z \in [0,L]$;
Calculate $\varphi_z(z)$ with equation (49b);
while $err > \epsilon$ **and** $i > max\_iter$ **do**
    Calculate $\varphi_r^{i+1}(r,z)$ by solving equation (46a) with equation (46b) $\forall z \in [0,L]$;
    Calculate integrals (47b) with φ_z, u^i, p^i and φ_r^{i+1}
    Calculate $Q_\pm^{i+1}(z)$ by solving equation (47a) with (47b) and (47c);
    Calculate $c_\pm^{i+1}(r,z) = Q_\pm^{i+1}(z)\mathrm{e}^{\mp\varphi_r^{i+1}(r,z)}$;
    Calculate $\varphi^{i+1}(r,z) = \varphi_z(z) + \varphi_r^{i+1}(r,z)$;
    Calculate $u^{i+1}(r,z)$ with equations (51a) –(51c);
    Calculate $p^{i+1}(r,z)$ with equations (50a) – (50k);
    $err = max(\|Q_+^{i+1} - Q_+^i\|_{max}, \|Q_-^{i+1} - Q_-^i\|_{max})$;
    $i = i + 1$;
end while
Calculate $I_\pm$ using (52a).

The postprocessing and calculation of integrals is done using Python.

E Parameter values

The general physical constants, reference quantities and dimensionless parameters used for all simulations in this work are given in Table 1. Values for length, radius and boundary values that where changed for the different examples are given in separate tables. Specific parameters for the trumpet shaped pores in Section 5.2 are given in Table 2. The parameters for Section 5.1 are given in Table 3 and the ones for Section 5.3 are given in Table 4.

Table 1: Parameter values used for all simulations.

Symbol	**Meaning**	**Value**	**Unit**
T	temperature	298.15	K
e_0	elementary charge	1.602e-19	C
k_B	Boltzmann constant	1.380e-23	$\mathrm{J\,K^{-1}}$
N_A	Avogadro constant	6.022e23	$\mathrm{mol^{-1}}$
$F = e_0 N_A$	Faraday constant	9.648e4	$\mathrm{C\,mol^{-1}}$
$R_G = k_B N_A$	Gas constant	8.314	$\mathrm{J\,mol^{-1}\,K^{-1}}$
ε_0	vacuum permittivity	8.854e-12	$\mathrm{F\,m^{-1}}$
$\varepsilon_r = 1 + \chi$	relative permittivity	78.49	-
ν	viscosity	0.8904e-3	$\mathrm{Pa\,s}$
c^R	ref. concentration	1	$\mathrm{mol\,L^{-1}}$
q^R	ref. charge	0.16	$\mathrm{C\,m^{-2}}$
D^R	ref. diffusion coeff.	1e-9	$\mathrm{m^2\,s^{-1}}$
R_0	ref. radius	1e-9	m
φ^R	ref. potential	0.25	V
p^R	ref. pressure	24.8	bar
γ	-	9.23	-
Λ	Debye length	0.4	-

Table 2: Parameter values used for the simulations of a trumpet shaped pore.

Symbol	Meaning	Value	Unit
L_0	ref. length	1e-7	m
δ	ratio radius and length	0.01	-
v^R	ref. velocity	0.0278	$\mathrm{m\,s^{-1}}$
P_e	Péclet number	2.78	-
I^R	ref. current	9.65e-13	A
Q^R_{eo}	ref. flow rate	2.78e-20	$\mathrm{m^3\,s^{-1}}$
L	length	10	-
L_1, L_2	length for surface charge	$0.1L$, $L - L_2$	-
R_1	maximum radius	10	-
R_2	minimum radius	1.5	-
k_+, k_-	diffusion coefficients	1.33, 0.79	-
c^{out} , c^{in}	bulk concentrations	0.1, 0.1	-
q	surface charge	1.0	-
φ^{out}, φ^{in}	bulk potential	8.0, 0.0	-
p^{out} , p^{in}	bulk pressure	0.0, 0.0	-

Table 3: Parameter values used for the simulations of EOF transitions in a cylindrical pore.

Symbol	Meaning	Value	Unit
L_0	ref. length	1e-8	m
δ	ratio radius and length	0.1	-
v^R	ref. velocity	0.278	$\mathrm{m\,s^{-1}}$
P_e	Péclet number	2.78	-
I^R	ref. current	9.65e-12	A
Q^R_{eo}	ref. flow rate	2.78e-19	$\mathrm{m^3\,s^{-1}}$
L	length	25	-
L_1, L_2	length for surface charge	$0.2L$, $L - L_2$	-
R	radius	5	-
k_+, k_-	diffusion coefficients	1.33, 0.79	-
c^{out} , c^{in}	bulk concentrations	0.6, 0.6	-
q	surface charge	0.15	-

Table 4: Parameter values used for the simulations of a ClyA pore.

Symbol	**Meaning**	**Value**	**Unit**
L_0	ref. length	1e-8	m
δ	ratio radius and length	0.1	-
v^R	ref. velocity	0.278	$\mathrm{m\,s^{-1}}$
P_e	Péclet number	2.78	-
I^R	ref. current	9.65e-12	A
Q_{eo}^R	ref. flow rate	2.78e-19	$\mathrm{m^3\,s^{-1}}$
L	length	5.5	-
L_1, L_2	length for surface charge	2.0, 3.5	-
R_1	maximum radius	5	-
R_2	minimum radius	1.65	-
k_+, k_-	diffusion coefficients	1.334, 2.032	-
q	surface charge	-0.25	-
p^{out} , p^{in}	bulk pressure	0.0, 0.0	-